The Astrophysical Journal Letters, 979:L30 (25pp), 2025 February 1 https://doi.org/10.3847/2041-8213/ada7f5

Characterization of a Peculiar Einstein Probe Transient EP240408a: An Exotic Gamma-Ray Burst or an Abnormal Jetted Tidal Disruption Event?

Brendan O'Connor[1,38], Dheeraj Pasham[2], Igor Andreoni[3,4,5,6], Jeremy Hare[7,8,9], Paz Beniamini[10,11,12], Eleonora Troja[13], Roberto Ricci[13,14], Dougal Dobie[15,16], Joheen Chakraborty[2], Mason Ng[17,18], Noel Klingler[7,8,19], Viraj Karambelkar[20], Sam Rose[20], Steve Schulze[21], Geoffrey Ryan[22], Simone Dichiara[23], Itumeleng Monageng[24,25], David Buckley[24,25,26,27], Lei Hu[1], Gokul P. Srinivasaragavan[3,4,7], Gabriele Bruni[28], Tomás Cabrera[1], S. Bradley Cenko[3,7], Hendrik van Eerten[29], James Freeburn[30,31], Erica Hammerstein[32], Mansi Kasliwal[20], Chryssa Kouveliotou[12], Keerthi Kunnumkai[1], James K. Leung[33,34,35], Amy Lien[36], Antonella Palmese[1], and Takanori Sakamoto[37]

[1] McWilliams Center for Cosmology and Astrophysics, Department of Physics, Carnegie Mellon University, Pittsburgh, PA 15213, USA; boconno2@andrew.cmu.edu
[2] MIT Kavli Institute for Astrophysics and Space Research, Cambridge, MA 02139, USA
[3] Joint Space-Science Institute, University of Maryland, College Park, MD 20742, USA
[4] Department of Astronomy, University of Maryland, College Park, MD 20742, USA
[5] Astrophysics Science Division, NASA Goddard Space Flight Center, Mail Code 661, Greenbelt, MD 20771, USA
[6] University of North Carolina at Chapel Hill, 120 E. Cameron Ave., Chapel Hill, NC 27514, USA
[7] Astrophysics Science Division, NASA Goddard Space Flight Center, 8800 Greenbelt Rd, Greenbelt, MD 20771, USA
[8] Center for Research and Exploration in Space Science and Technology, NASA/GSFC, Greenbelt, MD 20771, USA
[9] The Catholic University of America, 620 Michigan Ave., N.E. Washington, DC 20064, USA
[10] Department of Natural Sciences, The Open University of Israel, P.O Box 808, Ra'anana 4353701, Israel
[11] Astrophysics Research Center of the Open University (ARCO), The Open University of Israel, P.O Box 808, Ra'anana 4353701, Israel
[12] Department of Physics, The George Washington University, Washington, DC 20052, USA
[13] Department of Physics, University of Rome "Tor Vergata", via della Ricerca Scientifica 1, I-00133 Rome, Italy
[14] INAF-Istituto di Radioastronomia, Via Gobetti 101, I-40129 Bologna, Italy
[15] Sydney Institute for Astronomy, School of Physics, The University of Sydney, New South Wales 2006, Australia
[16] ARC Centre of Excellence for Gravitational Wave Discovery (OzGrav), Hawthorn, Victoria, Australia
[17] Department of Physics, McGill University, 3600 rue University, Montréal, QC H3A 2T8, Canada
[18] Trottier Space Institute, McGill University, 3550 rue University, Montréal, QC H3A 2A7, Canada
[19] Center for Space Sciences and Technology, University of Maryland, Baltimore County, Baltimore, MD 21250, USA
[20] Division of Physics, Mathematics and Astronomy, California Institute of Technology, Pasadena, CA 91125, USA
[21] Center for Interdisciplinary Exploration and Research in Astrophysics (CIERA), Northwestern University, 1800 Sherman Ave, Evanston, IL 60201, USA
[22] Perimeter Institute for Theoretical Physics, Waterloo, Ontario N2L 2Y5, Canada
[23] Department of Astronomy and Astrophysics, The Pennsylvania State University, 525 Davey Lab, University Park, PA 16802, USA
[24] South African Astronomical Observatory, P.O. Box 9, Observatory 7935, Cape Town, South Africa
[25] Department of Astronomy, University of Cape Town, Private Bag X3, Rondebosch 7701, South Africa
[26] Southern African Large Telescope, P.O. Box 9, Observatory 7935, Cape Town, South Africa
[27] Department of Physics, University of the Free State, P.O. Box 339, Bloemfonein 9300, South Africa
[28] INAF – Istituto di Astrofisica e Planetologia Spaziali, via del Fosso del Cavaliere 100, Roma, 00133, Italy
[29] Department of Physics, University of Bath, Claverton Down, Bath, BA2 7AY, UK
[30] Centre for Astrophysics and Supercomputing, Swinburne University of Technology, John St, Hawthorn, VIC 3122, Australia
[31] ARC Centre of Excellence for Gravitational Wave Discovery (OzGrav), John St, Hawthorn, VIC 3122, Australia
[32] Department of Astronomy, University of California, Berkeley, CA 94720-3411, USA
[33] David A. Dunlap Department of Astronomy and Astrophysics, University of Toronto, 50 St. George Street, Toronto, ON M5S 3H4, Canada
[34] Dunlap Institute for Astronomy and Astrophysics, University of Toronto, 50 St. George Street, Toronto, ON M5S 3H4, Canada
[35] Racah Institute of Physics, The Hebrew University of Jerusalem, Jerusalem 91904, Israel
[36] University of Tampa, Department of Physics and Astronomy, 401 W. Kennedy Blvd, Tampa, FL 33606, USA
[37] Department of Physics and Mathematics, Aoyama Gakuin University, 5-10-1 Fuchinobe, Chuo-ku, Sagamihara-shi Kanagawa 252-5258, Japan
Received 2024 October 28; revised 2024 December 23; accepted 2025 January 9; published 2025 January 27

Abstract

We present the results of our multiwavelength (X-ray to radio) follow-up campaign of the Einstein Probe transient EP240408a. The initial 10 s trigger displayed bright soft X-ray (0.5–4 keV) radiation with peak luminosity $L_X \gtrsim 10^{49}$ (10^{50}) erg s^{-1} for an assumed redshift $z \gtrsim 0.5$ (2.0). The Neil Gehrels Swift Observatory and Neutron star Interior Composition ExploreR discovered a fading X-ray counterpart lasting for ∼5 days (observer frame), which showed a long-lived (∼4 days) plateau-like emission ($t^{-0.5}$) before a sharp power-law decline (t^{-7}). The plateau emission was in excess of $L_X \gtrsim 10^{46}$ (10^{47}) erg s^{-1} at $z \gtrsim 0.5$ (2.0). Deep optical and radio observations resulted in nondetections of the transient. Our observations with Gemini South revealed a faint potential host galaxy ($r \approx 24$ AB mag) near the edge of the X-ray localization. The faint candidate host, and lack of other

[38] McWilliams Fellow.

potential hosts ($r \gtrsim 26$ AB mag; $J \gtrsim 23$ AB mag), imply a higher redshift origin ($z \gtrsim 0.5$), which produces extreme X-ray properties that are inconsistent with many known extragalactic transient classes. In particular, the lack of a bright gamma-ray counterpart, with the isotropic-equivalent energy (10–10,000 keV) constrained by GECam and Konus-Wind to $E_{\gamma,\rm iso} \lesssim 4 \times 10^{50}$ (6×10^{51}) erg at $z \approx 0.5$ (2.0), conflicts with known gamma-ray bursts of similar X-ray luminosities. We therefore favor a jetted tidal disruption event as the progenitor of EP240408a at $z \gtrsim 1.0$, possibly caused by the disruption of a white dwarf by an intermediate-mass black hole. The alternative is that EP240408a may represent a new, previously unknown class of transient.

Unified Astronomy Thesaurus concepts: X-ray astronomy (1810); X-ray transient sources (1852); Relativistic jets (1390); Gamma-ray bursts (629); Black holes (162)

1. Introduction

The extragalactic high-energy transient sky, spanning from X-rays to gamma rays, is a diverse collection of phenomena with timescales typically ranging from seconds to days. Among the most common are gamma-ray bursts (GRBs; C. Kouveliotou et al. 1993), which arise either from the merger of two compact objects (B. P. Abbott et al. 2017; V. Savchenko et al. 2017; A. Goldstein et al. 2017) or the collapse of massive stars (S. E. Woosley 1993; A. I. MacFadyen & S. E. Woosley 1999). GRBs exhibit two distinct phases: an initial prompt gamma-ray emission lasting typically on the order of seconds to tens of seconds (C. Kouveliotou et al. 1993), and an afterglow produced by the newly launched jet and its interaction with the surrounding medium (P. M észáros & M. J. Rees 1997; R. A. M. J. Wijers & T. J. Galama 1999).

Dedicated space telescopes such as Fermi (C. Meegan et al. 2009) and Swift (N. Gehrels et al. 2004) have revolutionized the field. With hundreds of high-energy transients detected by these missions, some have displayed unusual behaviors. For instance, many GRBs exhibit an extended plateau phase following the prompt emission, lasting from a few hundred seconds to several hours before rapidly declining in X-rays (e.g., B. Zhang et al. 2006; E. Troja et al. 2007; A. Rowlinson et al. 2010). This plateau phase is thought to result from long-lived central engine activity, potentially due to the spin-down of a newborn magnetar's dipole field (B. Zhang et al. 2006; E. W. Liang et al. 2006; E. Troja et al. 2007; N. Lyons et al. 2010; B. D. Metzger et al. 2011; A. Rowlinson et al. 2010; A. Rowlinson et al. 2013), though other interpretations exist (R. Shen & C. D. Matzner 2012; P. C. Duffell & A. I. MacFadyen 2015; P. Beniamini & R. Mochkovitch 2017; P. Beniamini et al. 2017, 2020a; G. Oganesyan et al. 2020; H. Dereli-Bégué et al. 2022).

In 2011, Swift identified three peculiar gamma-ray transients, later found to have long-lasting X-ray emission, with peak X-ray luminosities of 10^{47-49} erg s^{-1} at a few days after discovery, several orders of magnitude higher than typical GRB afterglows at a similar time (J. S. Bloom et al. 2011; A. J. Levan et al. 2011; D. N. Burrows et al. 2011; B. A. Zauderer et al. 2011; D. N. Burrows et al. 2011; S. B. Cenko et al. 2012; G. C. Brown et al. 2015; D. R. Pasham et al. 2015). These events also featured prolonged high-energy activity, lasting months instead of hours —far exceeding the duration of the longest GRB plateau phases (e.g., A. J. Levan et al. 2014; A. Cucchiara et al. 2015). These systems have been hypothesized to be relativistic jetted tidal disruption events (TDEs) where a star is disrupted by a massive black hole and the resulting jet is fortuitously pointed along our line of sight akin to a blazar (J. S. Bloom et al. 2011; A. J. Levan et al. 2011; S. B. Cenko et al. 2012; I. Andreoni et al. 2022; D. R. Pasham et al. 2023; L. Rhodes et al. 2023; Y. Yao et al. 2024).

The launch of the Einstein Probe (EP; W. Yuan et al. 2015, 2022) has opened a new window into the soft X-ray Universe, especially for fast transients. The Wide-field X-ray Telescope (WXT), with a field of view of approximately 3,600 deg^2, monitors soft X-rays in the 0.5–4 keV range. Since 2024 February, EP has detected a variety of intriguing fast X-ray transients (C. Zhang et al. 2024). While a number of fast transients discovered by EP have turned out to be Galactic (e.g., stellar flares or X-ray binaries) in nature (e.g., S. B. Potter et al. 2024; T. M. Gaudin et al. 2024), there is a variety that shows clear GRB-like properties (e.g., EP240315a/GRB 240315C, A. J. Levan et al. 2024; Y. Liu et al. 2024; J. H. Gillanders et al. 2024; R. Ricci et al. 2024; EP240414a, S. Srivastav et al. 2024; J. N. D. van Dalen et al. 2024; J. S. Bright et al. 2024; H. Sun et al. 2024) or has been associated with GRBs in a post-trigger, ground-based analysis (e.g., Y.-H. I. Yin et al. 2024; Y. Liu et al. 2024).

In this Letter, we present a multiwavelength (ultraviolet, optical, near-infrared, radio, X-ray, and gamma ray) study of the EP discovered X-ray transient EP240408a. EP240408a has properties distinct from any previously known high-energy transient. We argue that it is likely extragalactic in nature and has properties that are challenging to explain either as a GRB or jetted TDE.

The manuscript is laid out as follows. In Section 2, we highlight the results of the X-ray, ultraviolet, optical, near-infrared, and radio data obtained for EP240408a. We analyze the multiple possible interpretations for EP240408a in Section 3 and present our conclusions in Section 4.

All upper limits are presented at the 3σ level and all magnitudes are in the AB photometric system. We use a flat cosmology (Planck Collaboration et al. 2020). We further adopt the standard convention $F_\nu \propto \nu^{-\beta} t^{-\alpha}$.

2. Data Reduction and Analysis

2.1. EP Trigger and Gamma-Ray Constraints

The WXT on board the EP (W. Yuan et al. 2015, 2022) discovered EP240408a at 2024-04-08 at 17:56:30 UT or MJD 60408.747[39](J. W. Hu et al. 2024a). The peak flux and average flux in the soft X-ray (0.5–4.0 keV) band over the $\sim$10 s duration were reported to be $\sim 1.4 \times 10^{-8}$ erg s^{-1} cm^{-2} and $(4.0 \pm 1.3) \times 10^{-9}$ erg cm^{-2} s^{-1}, respectively (J. W. Hu et al. 2024a). This roughly translates to a soft X-ray fluence of $\sim 4 \times 10^{-8}$ erg cm^{-2}.

EP240408a was not detected or localized by any other high-energy monitor. Konus-Wind (R. L. Aptekar et al. 1995) and GECam (C. Li et al. 2023) were observing the location of EP240408a at the time of the EP trigger, but did not detect any

[39] All times in this work are relative to this trigger time.

emission (Dmitry Svinkin, private communication). The Fermi Gamma-ray Burst Monitor (GBM; C. Meegan et al. 2009) and AstroSat/CZTI (V. Bhalerao et al. 2017) have no data covering the location of EP240408a at the EP trigger time, while EP240408a was out of the field of view of Swift's Burst Alert Telescope (BAT; S. D. Barthelmy et al. 2005) (Jimmy DeLaunay/Swift and Gaurav Waratkar/Astrosat, private communication).

Konus-Wind was observing the position of EP240408a for 1000 s before and after the trigger time. The 90% confidence upper limit to the peak flux (20–1500 keV) is $<1.5 \times 10^{-7}$ erg cm^{-2} s^{-1} for a typical long GRB spectrum and assuming a timescale of 2.944 s (Dmitry Svinkin, private communication). This is consistent with the typical fluence upper limits for Konus-Wind based on all-sky searches for GRBs associated with gravitational waves (GWs), which have typical limits of $<6 \times 10^{-7}$ erg cm^{-2} and $< 2 \times 10^{-7}$ erg cm^{-2} for short and long GRBS, respectively, in the 20–1500 keV energy range (A. Ridnaia et al. 2020). GECam-B reported a slightly less sensitive 3σ upper limit of $<2.4 \times 10^{-6}$ erg cm^{-2} for the gamma-ray fluence in the 15–300 keV energy range (C.-W. Wang et al. 2024).

Despite being out of the field of view of Swift/BAT, and therefore lacking event data, the `NITRATES` pipeline (J. DeLaunay & A. Tohuvavohu 2022) can constrain the gamma-ray properties. The upper limit to the peak flux is $<3.4 \times 10^{-7}$ erg cm^{-2} s^{-1} for a 3.2 s timescale in the 15–350 keV energy band, corresponding to $<5.5 \times 10^{-7}$ erg cm^{-2} s^{-1} over 20–1500 keV for comparison to Konus-Wind (Jimmy DeLaunay, private communication).

We further ran the Swift/BAT Hard X-ray Transient Monitor (H. A. Krimm et al. 2013) source detection (15–50 keV) and light-curve production algorithm for a period corresponding to approximately 1 month before to 2 months after the EP trigger (MJD 60374–60461) and found no significant detections in the daily binned light curve. The source was out of the BAT field of view from approximately -19 to -4 days prior to the EP trigger.

2.2. Swift/XRT

The position of EP240408a was observed by the Neil Gehrels Swift Observatory (hereafter Swift; N. Gehrels et al. 2004) X-ray Telescope (XRT; D. N. Burrows et al. 2005) starting on 2024 April 10 (1.4 days after the EP trigger; J. W. Hu et al. 2024b). In total, observations were obtained across 5 epochs between 2024 April 10 and 2024 April 26 in photon counting (PC) mode for a total of 8.9 ks, see Table A1. An X-ray source is detected only in the first observation at 1.4 days with a total exposure of 1.8 ks in PC mode. The following XRT observations at 10.4, 12.4, 15.4, and 17.5 days (lasting between 1 and 2.5 ks) after the EP trigger did not result in a detection of the X-ray source. We used the Swift/XRT data products generator[40] and upper limit server[41] (P. A. Evans et al. 2023) to produce 3σ upper limits on the unabsorbed X-ray flux.

Swift/XRT data taken 1.4 days after the EP trigger yielded a standard position (P. A. Evans et al. 2009) of R.A., decl. (J2000) = $10^{h}35^{m}24^{s}.28$, $-35°44'49''.9$ with an uncertainty of $3''.5$ (90% confidence level; CL). However, a more refined enhanced position (M. R. Goad et al. 2007; P. A. Evans et al. 2009) is derived as R.A., decl. (J2000) = $10^{h}35^{m}23^{s}.96$, $-35°44'55''.1$ with an uncertainty of $2''.2$ (90% CL). The enhanced position shifts by $\sim 6''.5$ with respect to the initially reported standard position (Wenda Zhang, private communication).

2.3. NICER

EP240408a was monitored by the Neutron star Interior Composition ExploreR (NICER) using the X-ray timing instrument (XTI; K. C. Gendreau et al. 2016) between 2024 April 10 (MJD 60410.564) and 2024 May 16 (MJD 60447.259), corresponding to 1.8–38 days after trigger, with a near daily cadence (ObsIDs 7204340101 to 7204340131; Table A1). During this period NICER made several visits per day that typically lasted for a few hundred seconds. This resulted in an on-source exposure time of 109 ks. The initial 4 days of data were first reported in N. Rea et al. (2024a), and have been reanalyzed here along with the full data set.

We retrieved the data from the NICER data archive. The data were processed using `NICERDAS v12` within `HEASoft v6.34` and the latest calibration files. After retrieving the latest geomagnetic data, we processed the `nicerl2` task to generate cleaned event files with the default screening criteria. The late-time data was severely impacted by increased solar activity and all data was impacted by a significant oxygen line from Earth's atmosphere. We attribute this to significant background fluctuations due to solar activity and the atmospheric oxygen line, which we discuss further in Section 2.12.

NICER data consisted of both the International Space Station's nighttime and daytime data. As per the NICER data analysis guide,[42] for each ObsID, we extracted separate "clean" event files for both night and day data. Then, using the `nicerl3-spect` tool and the `SCORPEON` background modeling framework, we extracted separate night and day spectra from individual ObsIDs. We discuss our spectral modeling of the NICER data in Section 2.12.

2.4. NuSTAR

We observed EP240408a through a Director's Discretionary Time request (ObsID: 91001622; PI: O'Connor) for a total of 42 ks starting on 2024-04-22 at 00:36:09 UT ($T_0 + 13.3$ d). The data were reduced using the NuSTAR Data Analysis Software pipeline (`NuSTARDAS`) within `HEASoft v6.33.2`. At the location of EP240408a we do not detect a source in either FPMA or FPMB. As there are no sources detected in the image we cannot correct for the pointing accuracy of NuSTAR or any offsets between FPMA and FPMB. We extract the total observed counts using a $30''$ circular region centered on EP240408a and a nearby background region of $80''$ for both FPMA and FPMB. Using the formalism presented by R. P. Kraft et al. (1991), we derive a 3σ upper limit of $<1.4 \times 10^{-3}$ cts s^{-1} (3–79 keV). Adopting an absorbed power law with photon index $\Gamma = 2$ and hydrogen column density $N_{\rm H} = 1 \times 10^{21}$ cm^{-2}, we derive a 3σ upper limit of $<9.98 \times 10^{-14}$ erg cm^{-2} s^{-1} (3–79 keV) to the unabsorbed flux of EP240408a at $\sim$13.3 days after the EP trigger.

2.5. Archival X-Ray Data

We utilized the High-Energy light curve Generator (HILIGT; O. König et al. 2022; R. D. Saxton & M. Descalzo 2022)[43] to determine whether the source has experienced any archival

[40] https://www.swift.ac.uk/user_objects/
[41] https://www.swift.ac.uk/LSXPS/ulserv.php
[42] https://heasarc.gsfc.nasa.gov/docs/nicer/analysis_threads/
[43] http://xmmuls.esac.esa.int/upperlimitserver/

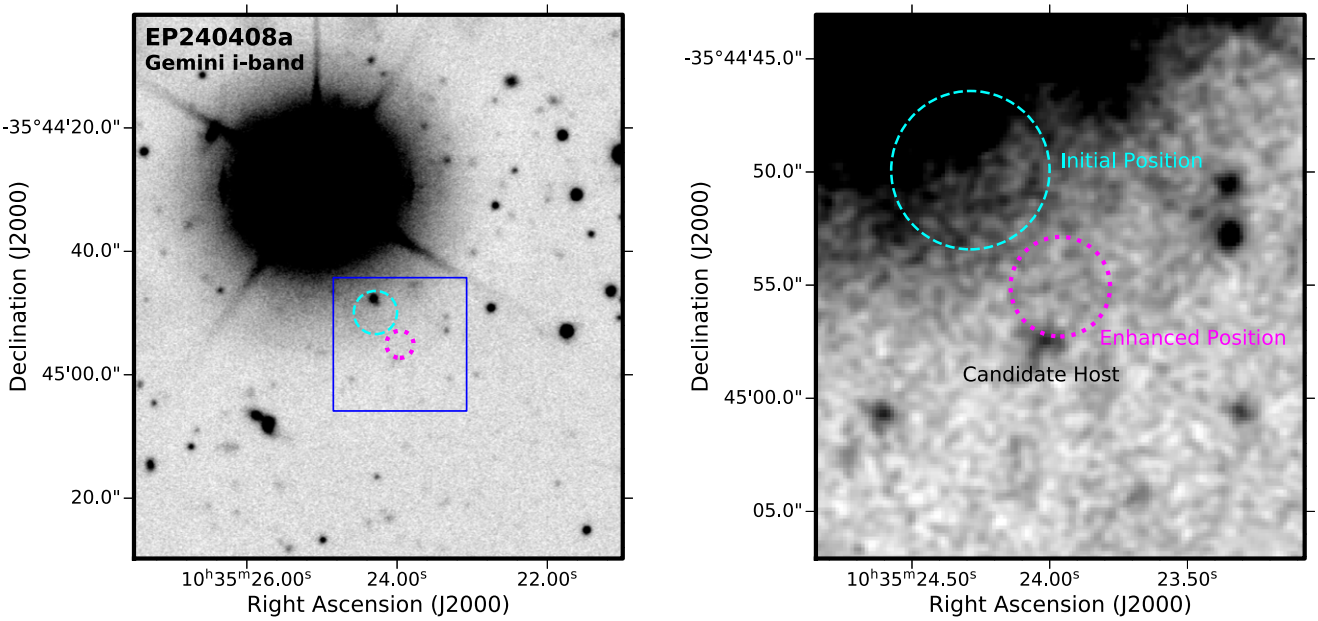

Figure 1. Left: finding Chart of EP240408a using deep images obtained with Gemini GMOS-S in the *i* band at $T_0 + 82$ days (2024 June 30) with 3σ limiting depth $\gtrsim$26 AB mag. The initial XRT localization (radius 3.″5; 90% CL) is shown as a cyan dashed circle. The enhanced XRT localization (radius 2.″2; 90% CL) is represented by a magenta dotted circle. The field of view of the zoom-in region (right panel) is shown by a blue square. Right: zoom-in on the enhanced localization of EP240408a. To the southeast of the enhanced position (dotted magenta circle) lies a candidate host galaxy. The image is smoothed for display purposes. North is up and east is to the left.

outburst potentially caught by ROSAT, INTEGRAL, or the XMM-Newton Slew Survey (e.g., R. D. Saxton et al. 2008). The source position was observed by XMM-Newton during slews six times between 2005 May 20 and 2024 May 18 with short ∼5–8 s exposures. Each observation has a similar limit in the three energy ranges (0.2–2, 2–12, and 0.2–12 keV), but the latest observation serendipitously occurred on 2024 May 18 at 21:34:05 UT, yielding a 3σ upper limit of $<2 \times 10^{-12}$ erg cm^{-2} s^{-1} in the 0.2–12 keV energy range. An absorbed power law with photon index $\Gamma = 2$ and hydrogen column density $N_{\rm H} = 1 \times 10^{20}$ cm^{-2} was used. The HILIGT also identified upper limits (3σ) from past ROSAT and INTEGRAL observations, assuming the same spectral shape, with $<2 \times 10^{-13}$ erg cm^{-2} s^{-1} (0.2–2 keV) from ROSAT on 1990 October 28 and $<7 \times 10^{-12}$ erg cm^{-2} s^{-1} (20–40 keV) from INTEGRAL on 2006 June 18. Therefore we have found no evidence for past X-ray outbursts from this source.

We likewise checked the eROSITA upper limit server[44] (D. Tubìn-Arenas et al. 2024). No source is detected at the location of the XRT source with 3σ upper limits $<6.7 \times 10^{-14}$ erg cm^{-2} s^{-1} (0.2–6 keV) and $<6.5 \times 10^{-14}$ erg cm^{-2} s^{-1} (0.2–2.3 keV). The nondetection in eROSITA was first reported by N. Rea et al. (2024b).

2.6. Gemini

We observed EP240408a with Gemini-South through a DDT request (GS-2024A-DD-104; PI: O'Connor) using the Gemini Multi-Object Spectrograph (GMOS) and FLAMINGOS-2 (F2). We carried out observations across three epochs on 2024 April 25, 2024 April 2, and 2024 June 30. We observed in the *riJ* filters with a total exposure of 720, 720, and 900 s for the first two epochs. The third epoch was performed only in *ri* filters for 960 and 1000 s, respectively. The third epoch serves as a template for image subtraction, and achieved the best observing conditions and seeing.

The data were reduced using standard tasks within the `Dragons` software package (K. Labrie et al. 2019, 2023), including using the `ultradeep` recipe for F2 images. At the southeast edge of the XRT-enhanced position, we identify a candidate host galaxy (Figure 1). In order to gauge variability between epochs, we performed difference imaging with the Saccadic Fast Fourier Transform (`SFFT`) software[45] (L. Hu et al. 2022). We performed image subtraction between all epochs for each filter and identified no optical or near-infrared variability in either the initial (standard) XRT position, the enhanced XRT position, or at the location of the candidate host galaxy. Our 3σ upper limits based on using our third epoch (2024 June 30) as the template for the *ri* filters and second epoch (2024 May 2) for the *J* band are reported in Table A2. Aperture photometry was performed using `SExtractor` (E. Bertin & S. Arnouts 1996) and photometric zero-points calibrated to the SkyMapper (S. C. Keller et al. 2007; C. Wolf et al. 2018) and Two Micron All Sky Survey (M. F. Skrutskie et al. 2006) catalogs.

To determine its nature and distance scale, we obtained spectroscopic observations of the bright source (A. Rau 2024), see Appendix C, lying within the initial (standard) XRT localization (Figure 1) using Gemini GMOS-S through program GS-2024A-FT-113 (PI. Andreoni) starting on 2024-06-30 at 23:59:20 UT. The data were acquired with the R400 grating with 2×1000 s exposure at central wavelength ∼8000 Å and 2×1000 s centered at ∼8200 Å. A 1″ slit width was used at a position angle of 127° chosen to minimize contamination from the nearby bright star. The data were reduced using `Dragons`. An inspection of the stacked 2D spectrum reveals no clear narrow emission lines in the observed wavelength range between

[44] https://erosita.mpe.mpg.de/dr1/erodat/upperlimit/single/

[45] https://github.com/thomasvrussell/sfft

~5700 and 10500 Å (Appendix C). The red end of the spectrum is severely impacted by bright sky emission lines.

2.7. Keck

A near-infrared spectrum of the bright source (A. Rau 2024), see Appendix C, within the initial standard XRT position was obtained with the Near-Infrared Echellette Spectrometer (J. C. Wilson et al. 2004) on the Keck II telescope starting on 2024 April 19 at 06:57:36 UT (10.54 days post-trigger). The spectrum (1.0–2.4 μm) was obtained at airmass 1.77 using the $0\farcs55$ slit with 4 × 300 s exposures. Data were reduced using standard reduction procedures within `pypeit` (J. Prochaska et al. 2020). The spectrum has a very low signal-to-noise ratio and is dominated by sky emission lines. We heavily rebinned the spectrum (9 pixels) and found no discernible features.

2.8. Swift/Ultra-Violet Optical Telescope

As described in Section 2.2, the Swift Ultra-Violet Optical Telescope (UVOT; P. W. A. Roming et al. 2005) observed EP240408a during the same time intervals as Swift/XRT due to its simultaneous instrument operation. The exposure time was split between the various optical/UV filters: *v*, *b*, *u*, *uvw*1, *uvm*2, and *uvw*2 (Table A2). We used a circular source extraction region centered on the XRT position with a radius of $3\farcs5$, which is the XRT positional uncertainty and a typical source extraction radius for faint sources. EP240408a was not detected in any observations nor in any filters. The upper limits are given in Table A2. For the background regions, we use a circular region of at least 20″ radius, placed near EP240408a's position. The exact position and size of the background region varies between observations, as it has to be placed differently in different/stacked observations in order to avoid image artifacts (e.g., readout streaks, smoke rings) caused by nearby bright sources which are roll-angle and pointing dependent, as well as bright sources and their large point-spread functions, which are present in some filters and not others. In order to obtain deeper limits, we also stacked all observations (of the same filter) from different epochs using the `HEASoft` tool `uvotimsum`. No source was detected, and these limits are given in Table A2.

2.9. Dark Energy Camera

We retrieved publicly available imaging obtained with the Dark Energy Camera (DECam). The data were obtained through the NOIRLab Astro Data Archive[46] (S. McManus & K. Olsen 2021). There is available imaging of the field of EP240408a in the *grz* filters (see Table A2 for details). Aperture photometry was performed using the `SExtractor` software and photometric zero-points calibrated to the Sky-Mapper catalog. We find no source at the location of the updated (enhanced) XRT localization or at the location of our candidate host galaxy (Figure 1).

2.10. Very Large Array

We carried out observations with the Karl J. Jansky Very Large Array (VLA) on 2024-04-19, 2024 September 13, and 2024 September 12 (24A-320; PI: O'Connor), see Table A3. The observations we performed in the *X* band with a central frequency of 10 GHz and a bandwidth of 4 GHz with the array in C configuration during the first observation (2024 April 19), B configuration on 2024 September 13, and A configuration on 2024 December 12. The time on source was ~24 minutes in both observations. The data were retrieved from the National Radio Astronomical Observatory archive, and processed using the VLA `CASA` pipeline in `CASA` v6.5.4 (J. P. McMullin et al. 2007). We used sources 3C286 and J1051-3138 as primary and phase calibrators. EP240408a does not show any radio emission (Table A3) with deep 3σ upper limits obtained with the VLA on 2024 April 19 (11 days), 2024 September 13 (158 days), and 2024 December 12 (258 days) of <17 μJy, <21 μJy, and <20 μJy, respectively.

2.11. Australia Telescope Compact Array

We observed the location of EP240408a with the Australia Telescope Compact Array (ATCA) between 2024-05-01T04:51:05 and 2024-05-01T10:32:05 (C3589; PI: Dobie). The observation was split into four groups of 2 × 12 minute observations across that period, for 96 minutes on-source in total. Observations were carried out with 2 × 2048 MHz bands centered on 5.5 and 9 GHz. We used an observation of the ATCA primary calibrator, 1934–638, as the bandpass and flux scale calibrator and 1034–374 as the gain calibrator. We carried out standard ATCA data reduction with `MIRIAD` (R. J. Sault et al. 1995) and found no emission at the transient location with a 3σ upper limit of 60 μJy in both bands.

EP240408a was also observed with the ATCA by an independent group under a target-of-opportunity program (CX570; PI: Shu) on two occasions. The first observation was conducted on 2024 May 08 with 2 × 2048 MHz bands centered on 5.5 and 9 GHz. The second observation was conducted on 2024 May 10 with 2 × 2048 MHz bands centered on 17 and 19 GHz. Neither observation has an associated observation of the ATCA primary calibrator (1934–638), nor were there any observations of it within a day of either observation. Hence, standard flux calibration of these observations is not possible. We have not analyzed the 2024 May 8 data because of this, and the proximity to our more sensitive observation on 2024 May 1.

Nevertheless, we reduced the data obtained on 2024 May 10 because it provides coverage at higher observing frequencies. We used 1034–293 as the flux and bandpass calibrator and 1048–313 as the gain calibrator. Both bands were reduced independently in `MIRIAD` and then scaled to have a consistent flux scale using `MFBOOT` before being combined and imaged as a single contiguous band. We do not detect any radio emission at the position of the transient. We set the absolute flux scale by setting the flux density of 1034–293 to 2 Jy based on its typical flux density in the ATCA calibrator database.[47] However, 1034–293 appears to be significantly variable (with previously observed flux densities ranging from 1 to 3 Jy) and hence this scaling is likely unreliable. Based on this calibration, the image noise is ~15 μJy, which is four times more sensitive than the noise estimate reported by the ATCA sensitivity calculator. We consider the ATCA sensitivity to be a more reliable (albeit, optimistic) estimate of the overall flux scale, and hence, we report a 3σ upper limit of 180 μJy on the source flux density for this observation.

[46] https://astroarchive.noirlab.edu/

[47] https://www.narrabri.atnf.csiro.au/calibrators/calibrator_database_viewcal?source=1034-293

2.12. X-Ray Spectroscopy

2.12.1. Swift/XRT

The first X-ray observation and detection following the initial EP trigger was by Swift/XRT approximately 1.4 days later (J. W. Hu et al. 2024b; A. D. Chandra 2024). We retrieved the XRT spectra using the Swift/XRT data products generator. The data were modeled in XSPEC (K. A. Arnaud 1996) using the C-statistic (W. Cash 1979). Previous reports of the spectra (J. W. Hu et al. 2024b; A. D. Chandra 2024) assumed redshift $z = 0$. For the same assumptions (a $z = 0$ absorbed power law; tbabs*pow), we confirm the prior reports of a hydrogen column density $N_{\rm H} = (1.4 \pm 0.5) \times 10^{21}$ cm^{-2}, photon index $\Gamma = 2.10 \pm 0.18$, and unabsorbed flux $F_{\rm X} = (2.5^{+0.3}_{-0.2}) \times 10^{-11}$ erg cm^{-2} s^{-1} in the 0.3–10 keV band.

Here, we model the data with an absorbed power-law model ztbabs*zashift*(clumin*pow), assuming either $z = 0.5$ or $z = 2$ due to the unknown distance (Section 3.1). For $z = 0.5$, we find $N_{\rm H} = (3.0 \pm 0.6) \times 10^{21}$ cm^{-2}, $\Gamma = 2.09 \pm 0.08$, and a 0.3–10 keV rest frame X-ray luminosity of $L_X = (5.85^{+0.40}_{-0.24}) \times 10^{46}$ erg s^{-1}. For $z = 2$, we instead derive $N_{\rm H} = (1.1 \pm 0.3) \times 10^{22}$ cm^{-2}, $\Gamma = 1.85 \pm 0.11$, and a 0.3–10 keV rest frame K-corrected X-ray luminosity of $L_X = (4.8 \pm 0.6) \times 10^{48}$ erg s^{-1}. We compare this to the NICER results below.

2.12.2. NICER

Here, we focus on the analysis of the full NICER data set of EP240408a. We introduced the NICER data set in Section 2.3. Here we provide a detailed description of the data extraction and analysis, specifically with regard to the spectra.

As per the NICER data analysis guide, for each ObsID, we extracted separate "clean" event files for both the nighttime and daytime data. We used the nicerl3-spect tool to extract separate night and day spectra from each ObsID. We started our spectral analysis by inspecting these spectra, several of which showed an excess in the 0.5–0.6 keV band. This is a known contamination issue originating from the foreground oxygen line complex from Earth's atmosphere. This can happen in both the daytime and nighttime data and at present, there is no tool provided by the NICER team to mitigate this problem.

In order to reduce contamination from the oxygen line, we designed the following methodology. First, we divided the entire NICER light curve into 18 subintervals whose boundaries were chosen based on the Bayesian blocks algorithm (J. D. Scargle et al. 2013) on the 0.3–10 keV light curve extracted from nicerl3-lc tool. We extract both nighttime and daytime spectra from each of the 18 Bayesian blocks, resulting in 36 X-ray spectra.

For each spectrum, we applied the following procedure. We ignored spectra with less than 300 s of exposure and only focus on the most reliable data. If the exposure is more than 300 s, we fit the spectrum in XSPEC (K. A. Arnaud 1996), using the C-statistic (W. Cash 1979), with the SCORPEON background model. Following the recommendation of the NICER team,[48] we fit the daytime and nighttime spectra in the 0.25–10 keV and 0.38–10 keV bands, respectively. We fit the spectrum twice: first allowing for the normalization of the oxygen K foreground emission line to vary and second with the normalization fixed to 0. We then use the Akaike information criterion (AIC) to determine whether there is significant contamination from the oxygen line (requiring $\Delta{\rm AIC} < -20$ between the two models).

We then fit the spectrum again using an absorbed power-law model ztbabs*zashift(clumin*pow), including an oxygen line if $\Delta{\rm AIC} < -20$ from the previous fit. In order to determine whether the source is detected in an individual spectrum, we require $\Delta{\rm AIC} < -20$ when comparing the fit with and without the power-law model in addition to the SCORPEON background model. We note that automated procedures within the NICERDAS software (e.g., nicerl3-lc) detect flaring periods at later times, but we determine these are due to the Earth's atmosphere (oxygen K emission). This is consistent with the deeper nondetections by Swift/XRT over similar time periods (see Table A1).

Some of the spectra yielded a reduced C-statistic of >2 for our power-law model, see the bottom panel in Figure 2. The ratio plots indicated the presence of a break in the spectrum. Thus, we followed the same methodology using ΔAIC for a broken power-law model (ztbabs*zashift(clumin*bknpow)) as well. We then compared the ΔAIC between the power-law (pow) and broken power-law (bknpow) models. We find a broken power law is the preferred model in epochs 3, 4, 5, 6, and 8 (referred to as, e.g., E3, E4, etc.). Using a broken power-law model resulted in reduced C-statistic values close to unity (Figure 2, bottom panel), without the significant residuals observed in the power-law-only model. This spectral break is observed in both day and night spectra.

For each spectral fit, we derived a count rate to unabsorbed K-corrected 0.3–10 keV luminosity conversion factor. We then use this to estimate a light curve (luminosity versus time) on a per good time interval basis. The light curve is shown in Figure 3.

Based on our spectral analysis (for $z = 0.5$), we find a typical hydrogen column density of $N_{\rm H} \approx (1.5\text{–}2.5) \times 10^{21}$ cm^{-2}, photon index $\Gamma_1 = 1.5\text{–}2.0$, and an observer frame spectral break at $E_{\rm break} \approx 4.5$ keV where the spectra steepens to $\Gamma_2 = 2.5\text{–}3.0$. The evolution of the spectral index is rather unconstrained by the data due to the decreasing source count statistics at higher energies and a variable background rate. The photon index Γ_1 and column density $N_{\rm H}$ are comparable to that derived from the initial Swift/XRT detection. There is marginal evidence that the photon index Γ_1 decreases from $\sim$2 to $\sim$1.5 over the first few days.

The NICER spectra also revealed the requirement of an intrinsic absorption component in excess of the Galactic value of $N_{\rm H,gal} = 8.5 \times 10^{20}$ cm^{-2} along the line of sight (R. Willingale et al. 2013). The expected optical extinction A_V from the inferred hydrogen column density $N_{\rm H} \approx (1.5\text{–}2.5) \times 10^{21}$ cm^{-2} is $A_V \approx 1$ mag at $z \approx 0.5$ (T. Güver & F. Özel 2009), with larger values required at higher redshifts (2.12).

2.13. NICER X-Ray Light Curve

NICER observed EP240408a at high cadence between 1.8 and 38 days post-trigger. The overall light curve shows a slow decline over the first few days followed by a rapid drop-off (see Figure 3). The count rate light curve decays from $\sim$8 cts s^{-1} to $\sim$5 cts s^{-1} over $\sim$2 days before steepening and rapidly fading below detection over the course of $\sim$1 day. We can model the count rate light curve with a broken power law of $t^{-0.5}$ breaking to t^{-5} around $\sim$4.1 to 4.3 days after the EP trigger. This steep break is seen in both daytime and nighttime data.

However, the luminosity light curve (see Section 2) is significantly steeper (t^{-7}; Figure 3) as it properly accounts for

[48] https://heasarc.gsfc.nasa.gov/docs/nicer/analysis_threads/cal-recommend/

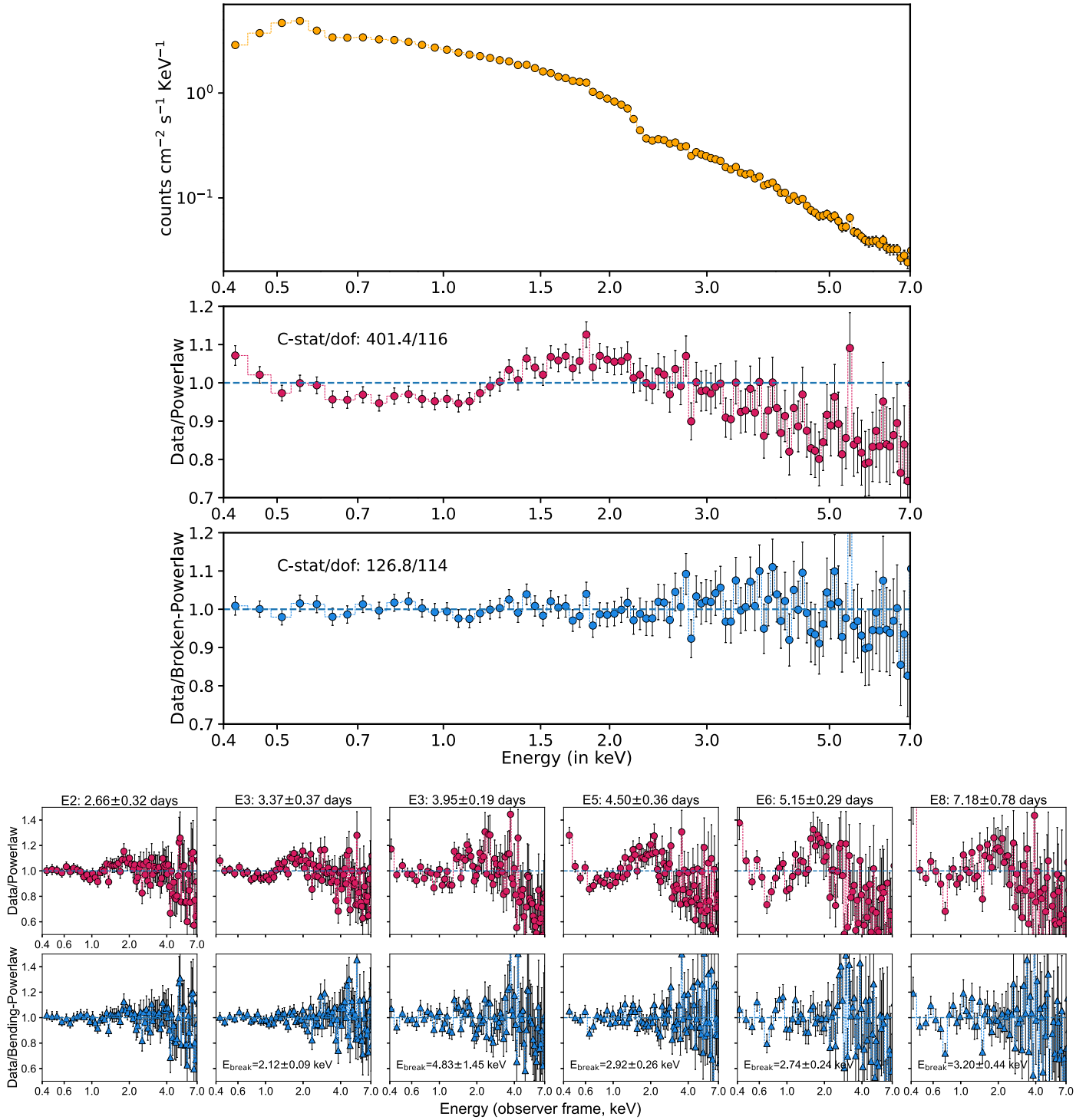

Figure 2. Top: time-averaged NICER spectrum of EP240408a using all data from MJD 60410.567515 to 60416.699. The top panel shows the logarithm of counts vs energy. The energy range where the source is above the SCORPEON background is shown, but the full 0.38–10.0 keV was used for fitting as per NICER data analysis guidelines. Middle: ratio (data to best-fit model) plots corresponding to a power-law and a broken power-law fit, respectively. Bottom: same as middle plots, now showing a summary of spectral modeling of early NICER spectra. The time from the EP trigger is shown at the top of each column. The top panels show the ratio of data to the best-fit power-law model, while the bottom panels are ratios of data to the best-fit broken power-law model. The break energy (in the rest frame) is listed in the bottom panels. These plots were generated using a redshift $z = 0.5$, but the residuals are similar for $z = 2.0$, though the rest frame location of the break is modified.

the background, in particular the oxygen line (Section 2.12.2). We used the `dynesty` (J. S. Speagle 2020) nested sampling package to fit the X-ray (0.3–10.0 keV) flux light curve with a broken power law, which yields a slope of $t^{-0.51\pm0.05}$ early-on, which breaks to $t^{-6.7\pm0.2}$ around an observer frame time of 4.19 ± 0.02 days post-trigger. We infer a timescale $\delta\tau/\tau \approx 0.2$ for the plateau's decline.

We briefly consider other possible explosion times for EP240408a, prior to the EP trigger. If we allow for an explosion (or disruption; depending on interpretation) time of

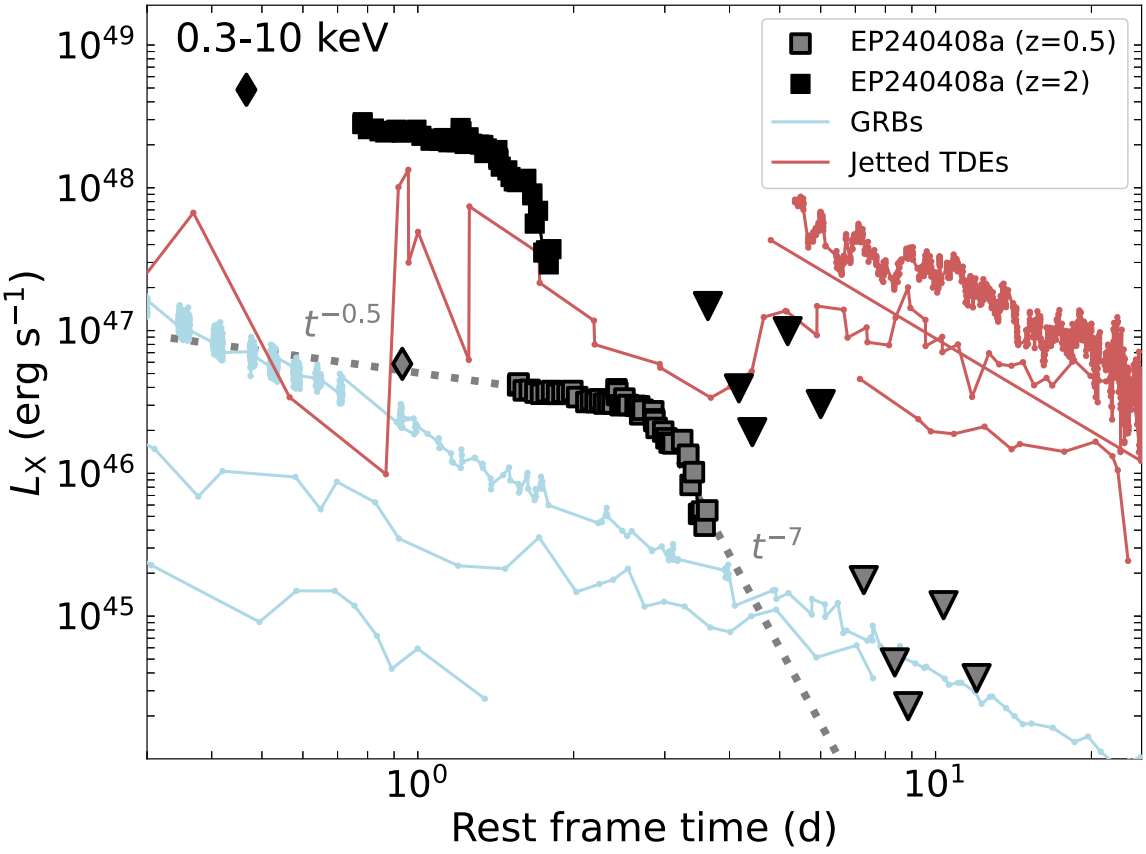

Figure 3. Comparison between the rest frame (0.3–10 keV; K-corrected) X-ray light curve of EP240408a (black) at different assumed redshifts ($z = 0.5$ and 2) vs. a sample of luminous GRBs in blue (GRB 070110, GRB 221009A, and EP240315), and jetted TDEs in red (J. S. Bloom et al. 2011; A. J. Levan et al. 2011; S. B. Cenko et al. 2012; G. C. Brown et al. 2015; D. R. Pasham et al. 2023). NICER data of EP240408a are shown by squares, and Swift data by a diamond for the first detection at 1.4 days and upper limits from Swift and NuSTAR as downward triangles. All data and limits are in the rest frame 0.3–10 keV energy range. The gray dotted lines show a broken power law with an initial slope of $t^{-0.5}$ breaking to t^{-7} at ~4.2 days in the observer frame. Figure reproduced from D. R. Pasham et al. (2023).

~3 days prior to the trigger the light curve can be roughly modeled with a broken power law of $t^{-5/3}$ and t^{-15}. If taken to be 10 days prior, these slopes are instead $t^{-2.2}$ and t^{-25} with the break occurring at ~14.1–14.3 days (observer frame). It is possible for EP to miss the X-ray transient in prior observations accounting for natural variability of the X-ray light curve as shown by Sw J1644+57 at early times. However, the significant difficulty in this case is explaining the EP trigger as a ~1000 × brighter flare at ~3–10 days after the initial onset.

3. Discussion

3.1. An Optical Search Reveals a Potential Host

Our deep Gemini imaging (Section 2.6) uncovers a candidate host galaxy at the southeast edge of the updated XRT-enhanced localization (Figure 1). We detect this source only in our optical *r*-band and *i*-band images with brightness $r \approx 24$ AB mag (Table A2). The source is not detected in our near-infrared imaging to depth $J \gtrsim 23.2$ AB mag. As we detect this source only in two filters, no robust constraints on its spectral energy distribution or distance scale can be obtained, and there is no existing optical or near-infrared spectroscopy of this source. We performed difference imaging between the Gemini observation epochs with the `SFFT` software (L. Hu et al. 2022), but did not identify any optical or near-infrared variability near either the initial position, enhanced XRT position, or the location of this candidate host (Section 2.6 and Table A2).

The probability of chance coincidence P_{cc} of the candidate host with the 3σ XRT localization is $P_{cc} \approx 0.15$ (J. S. Bloom et al. 2002; E. Berger 2010a). This is generally considered an inconclusive association for an extragalactic transient. A typical cutoff for a conclusive association is $P_{cc} < 0.1$ (e.g., E. Berger 2010a; W. Fong et al. 2013; W.-f. Fong et al. 2022; B. O'Connor et al. 2022). In this case, the lack of a subarcsecond localization prevents a robust determination, but we identify this source as the most likely host for EP240408a among the sources we are able to resolve in our deep optical and near-infrared images. If we expand our search for other potential host galaxies to all sources within ~90″ following the methods outlined in B. O'Connor et al. (2022), we find six clearly extended galaxies within this region with the closest offsets of 25–26″. We compute the probability of chance coincidence P_{cc} (J. S. Bloom et al. 2002; E. Berger 2010a) for these galaxies using their *r* band apparent after correcting for Galactic extinction $E(B-V) = 0.076$ mag (E. F. Schlafly & D. P. Finkbeiner 2011). Each of these galaxies has $P_{cc} > 0.6$–0.95 and all are unlikely hosts to EP240408a. We therefore conclude that EP240408a is extragalactic in nature and likely related to the faint galaxy lying at the edge of the XRT localization (Figure 1).

From Gemini, we have deep upper limits on any other underlying source within the XRT localization of $r > 26$,

$i > 26.1$, and $J > 23.2$ AB mag. These limits are capable of excluding the majority of GRB (e.g., J. T. Palmerio et al. 2019; B. Schneider et al. 2022; B. O'Connor et al. 2022; A. E. Nugent et al. 2022), and TDE (E. Hammerstein et al. 2021) host galaxies out to $z \sim 0.5$–1, and imply a higher redshift for EP240408a. The brightness of our candidate host galaxy, when compared to other high-energy extragalactic transient host galaxies, also potentially places it at higher redshifts $z \gtrsim 1$ in the range of 0.1–1.0L_* galaxies (see, e.g., B. O'Connor et al. 2022). However, we cannot exclude that it is a small galaxy ($10^{8-9}M_\odot$) at $z \approx 0.5$. For example, adopting galaxy correlations between the i-band absolute magnitude and stellar mass (E. N. Taylor et al. 2020), our observations are sensitive to a $10^8 M_\odot$ galaxy out to $z \approx 0.5$ and a $10^9 M_\odot$ galaxy out to $z \approx 2$. Future optical spectroscopy of this source can constrain its distance scale, though given its brightness, such observations are challenging. In what follows (Sections 3.3 and 3.4), we treat the distance scale of EP240408a as unconstrained and consider redshifts between $z \approx 0.5$ and 2. Lower redshifts are strongly disfavored by the lack of bright optical, near-infrared, or radio counterparts.

3.2. Disfavoring a Galactic Origin

Here, we argue that the observed brightness of the initial EP trigger strongly disfavors a Galactic nature for the source as the luminosity and other properties are inconsistent with Galactic transients such as cataclysmic variables (CVs), high-mass X-ray binaries (HMXBs), low-mass X-ray binaries (LMXBs), and Galactic magnetars.

The lack of a bright optical counterpart, evidence for a hydrogen column density larger than the line-of-sight Galactic value (see Section 2.12.2), lack of X-ray periodicity (Appendix B; N. Rea et al. 2024a), and smooth decline of the light curve lacking any short timescale X-ray variability, all strongly disfavor accreting binaries such as CVs, HMXBs, or LMXBs. The X-ray luminosity of the source at 20 kpc approaches $L_X \approx 10^{39}$ erg s^{-1} (0.5–4 keV), which would be at the high end of the luminosity function for XRBs, though not completely unreasonable. One reason to consider a Galactic scenario is that EP240408a is located at a relatively low Galactic latitude with Galactic coordinates $l, b = 274.16$ deg, 19.41 deg. However, as there is almost no Galactic dust in this field ($A_V \approx 0.2$ mag; E. F. Schlafly & D. P. Finkbeiner 2011), which could hide luminous Galactic objects, we should have detected a high-mass star in our Gemini images out to even >100 kpc, and M dwarf stars should be detected out to 15 kpc even in quiescence.

The lack of X-ray periodicity (Appendix B) and lack of a low-temperature X-ray spectrum (or blackbody excess) can also be used to strongly disfavor a Galactic magnetar as the origin of EP240408a. The archival X-ray limit on a quiescent X-ray flux from eROSITA (D. Tubìn-Arenas et al. 2024), assuming a distance of 1–10 kpc is $\lesssim 10^{31-33}$ erg s^{-1} (0.2–6 keV). For comparison, the observed quiescent X-ray luminosity for Galactic magnetars is in the range of 10^{30-35} erg s^{-1} (F. Coti Zelati et al. 2017).

An extensive literature search for similar light curves revealed that the X-ray outbursts of accreting millisecond X-ray pulsars (MSPs) display comparable behavior (R. Wijnands 2004). Their outbursts can be modeled by multiple exponential decays defined by $e^{-t/\tau}$, where the initial exponential decay timescale τ is typically on the order of 5–10 days and can steepen to a decay timescale of 1–2 days (M. Gilfanov et al. 1998; C. B. Markwardt et al. 2002; M. Falanga et al. 2005; P. G. Jonker et al. 2010; A. Sanna et al. 2018). The break time is usually around 10 − 20 days after discovery. We find EP240408a's X-ray luminosity light curve (Figure 3) can be fit with $e^{-t/6}$ breaking to $e^{-t/0.8}$ after ∼4 days. However, the major difference between transient MSP outbursts and EP240408a lies in the X-ray spectra. The MSP outbursts display spectral cutoff energies in excess of 100 keV, significantly higher than the ∼4 keV spectral break observed by NICER (Figure 2). We also found no evidence for periodicity in the X-ray data, even after performing an accelerated pulsar search (see Appendix B). For these reasons, we disfavor an MSP as the explanation for EP240408a. If EP240408a is Galactic in origin, which we disfavor, it would represent a peculiar, and potentially unique, X-ray transient.

3.3. Extragalactic Scenarios for EP240408a

We consider a number of possible extragalactic scenarios capable of explaining EP240408a's observed properties (high X-ray luminosity, sharp X-ray decay, and lack of optical or radio counterpart to deep limits).

3.3.1. Constraints on Prompt Gamma-Ray Emission

As EP240408a is likely a luminous extragalactic transient (peak X-ray luminosity $L_X \approx 10^{49}$ erg s^{-1} at $z = 0.5$; 0.5–4 keV), the natural first interpretation is a long-duration GRB. This is simply due to the frequently observed rate of long GRBs, approximately one per day detected by all-sky monitors such as Fermi and Swift, and the similar prompt timescale of ∼10 s. Moreover, since the launch of EP, there have been a number of likely GRBs that lack hard gamma-ray detections (e.g., Y.-H. I. Yin et al. 2024), though we note that given the soft X-ray trigger these are not effectively true "orphan" GRBs (E. Nakar et al. 2002; Y. F. Huang et al. 2002; N. Dalal et al. 2002).

In Figure 4 (left panel), we compare the constraints on the prompt gamma-ray energy (isotropic equivalent) from GECam-B and Konus-Wind to a population of long and short GRBs. We also show the estimated gamma-ray energy (10–10, 000 keV) for EP240408a adopting a typical range of long GRB prompt emission spectra ($E_p = 70$–300 keV; $\alpha = -1$; $\beta = -3$; D. Band et al. 1993). This comparison shows that there exist a variety of short and long GRBs consistent with the GECam-B limits, but that the expected Konus-Wind limits are only marginally consistent with the expected prompt emission of EP240408a (if interpreted as a GRB).

A more informative diagnostic comes from combining limits on the prompt emission with observations of the X-ray afterglow. A standard diagnostic is the ratio of the X-ray flux at 11 hr $F_{X,11}$ to the gamma-ray fluence ϕ_γ (M. Nysewander et al. 2009; E. Berger 2014; B. O'Connor et al. 2020, 2022; Y.-H. Yang et al. 2024; D. A. Perley et al. 2024), which is approximately distance independent with only a slight correction for redshift (see B. O'Connor et al. 2020, for a discussion). We find that E240408a has a high ratio $F_{X,11}/\phi_\gamma > 10^{-5}$, already higher than the most luminous GRBs (e.g., M. Nysewander et al. 2009; E. Berger 2014). This implies that the X-rays are very bright compared to any possible gamma-ray emission. We further show this in Figure 4 (right), which displays the X-ray luminosity at rest frame 11 hr $L_{X,11}$ versus the isotropic-equivalent gamma-ray energy. The allowed space

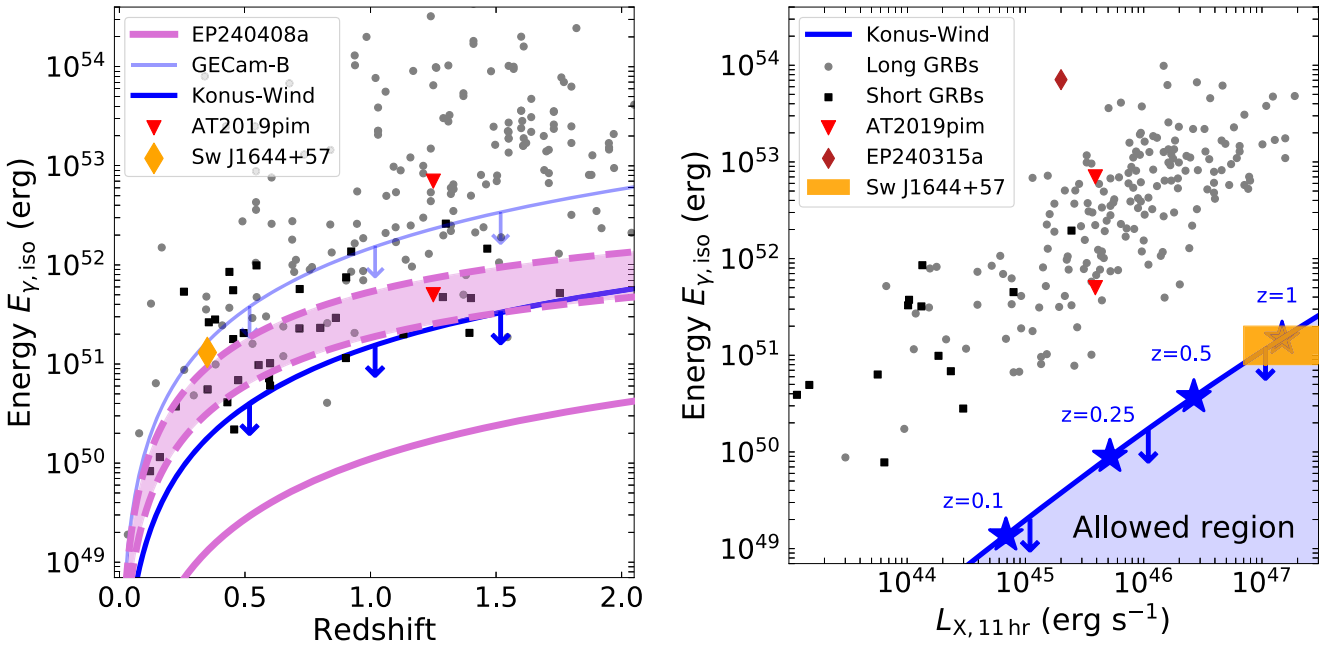

Figure 4. Left: distribution of isotropic-equivalent gamma-ray energies (10–10,000 keV) of both short (black squares) and long-duration (gray circles) GRBs versus redshift (T. Sakamoto et al. 2011a; A. Lien et al. 2016; J. L. Atteia et al. 2017; B. O'Connor et al. 2024). The approximate energy (0.5–4 keV) of the initial EP detection of EP240408a is shown by a thick purple line. Adopting a typical range of long GRB prompt emission spectra ($E_{\rm p}$ = 70–300 keV) we estimate the 10–10,000 keV gamma-ray energy of EP240408a (shaded region between purple dashed lines). This is compared to upper limits on the gamma-ray energy from GECam-B (solid light blue line) and Konus-Wind (solid dark blue line; Dmitry Svinkin, private communication). Reproduced from B. O'Connor et al. (2023). Right: rest frame X-ray luminosity (0.3–10 keV) at 11 hr versus gamma-ray energy (10–10,000 keV). A sample of short (black squares) and long GRBs (gray circles) are compiled from M. Nysewander et al. (2009); E. Berger (2014). Other strange GRBs such as EP240315a (A. J. Levan et al. 2024; Y. Liu et al. 2024) and AT2019pim (D. A. Perley et al. 2024) are also shown. We also display the approximate location of Sw J1644+57 (J. S. Bloom et al. 2011; A. J. Levan et al. 2011; D. N. Burrows et al. 2011) using the energy of the initial prompt gamma-ray trigger (T. Sakamoto et al. 2011b) converted to 10–10,000 keV (see text). The blue stars mark multiple redshifts up to z = 1, higher redshifts produce further tension with observed long GRBs. The solid blue line represents the luminosity of the Swift/XRT detection of EP240408a at 1.4 days (observer frame).

for EP204048a (blue-shaded region) is clearly separate from any short or long GRB at all redshifts, though the difference increases at $z > 1$. We note that this comparison would become even more significant if the X-ray luminosity at > 1 day was compared instead of the earlier time of 11 hr as the majority of GRBs decay as t^{-1}, whereas EP240408a displays a slower fading plateau-like decay.

The constraints on EP240408a (Figure 4) push it toward the region occupied by the relativistic jetted TDE Sw J1644+57 (J. S. Bloom et al. 2011; A. J. Levan et al. 2011). We converted the 15–150 keV fluence of the initial BAT trigger (T. Sakamoto et al. 2011b) of Sw J1644+57 to the 10–10,000 keV energy range assuming a peak energy of $E_{\rm p} \approx 70$ keV (A. J. Levan et al. 2011). We further consider the jetted TDE scenario in Section 3.6.

3.3.2. The Multiwavelength Properties of EP240408a

Here, we briefly compare the observed multiwavelength properties of EP240408a to other classes of high-energy extragalactic transients. A more detailed discussion of each transient class is presented in Section 3.4. We focus here on a few possible candidates, including GRBs, jetted TDEs, and fast blue optical transients (FBOTs).

Figure 3 compares the rest-frame X-ray (0.3–10 keV; K-corrected) light curve of EP240408a (assuming either redshifts $z \approx 0.5$ or 2.0) to GRBs and jetted TDEs. While the peak X-ray luminosity of GRBs can be orders of magnitude higher ($>10^{50}$ erg s^{-1}), jetted TDEs clearly separate themselves from long GRBs in their luminous, long-lasting X-ray emission. The X-ray emission of EP240408a is also more long-lived than a typical GRB, and for a redshift $z \approx 1$–3 appears to be consistent with the X-ray luminosity of jetted TDEs. We also note that the observed X-ray spectral break (Figure 2) is characteristic of nonthermal emission, and observed in both GRBs and jetted TDEs (e.g., AT2022cmc; Y. Yao et al. 2024); see Section 3.7 for further discussion of this point.

While we did not detect EP240408a in deep optical, near-infrared, or radio observations we can still compare these limits (focusing again on $z \approx 0.5$ or 2.0) to these classes of transients. In Figure 5 (right panel) we compare our Gemini limits to a variety of optical transients, finding that we can exclude most classes (e.g., GRBs, FBOTS, TDEs) out to $z \sim 0.5$ (and beyond), and significantly disfavoring a low redshift $z < 0.5$ for any of these classes. In addition, for $z < 0.5$, the inferred hydrogen column density predicts a decreasing intrinsic extinction $A_V < 1.4$ mag with decreasing redshift, making luminous optical emission even less likely to be missed. This further motivates considering higher redshift interpretations for EP240408a (see also Section 3.1).

In Figure 5 (left panel) we show the rest frame radio light curves of multiple well-known transients to our VLA and ATCA upper limits. Both jetted TDEs and long GRBs produce long-lasting luminous radio emission that should likely be detected out to $z \approx 2$. We discuss potential reasons for delayed radio emission from a jetted TDE in Section 3.6. We also explore the implications of a nondetection on the jet's kinetic energy and the density of the surrounding environment in Section 3.5.

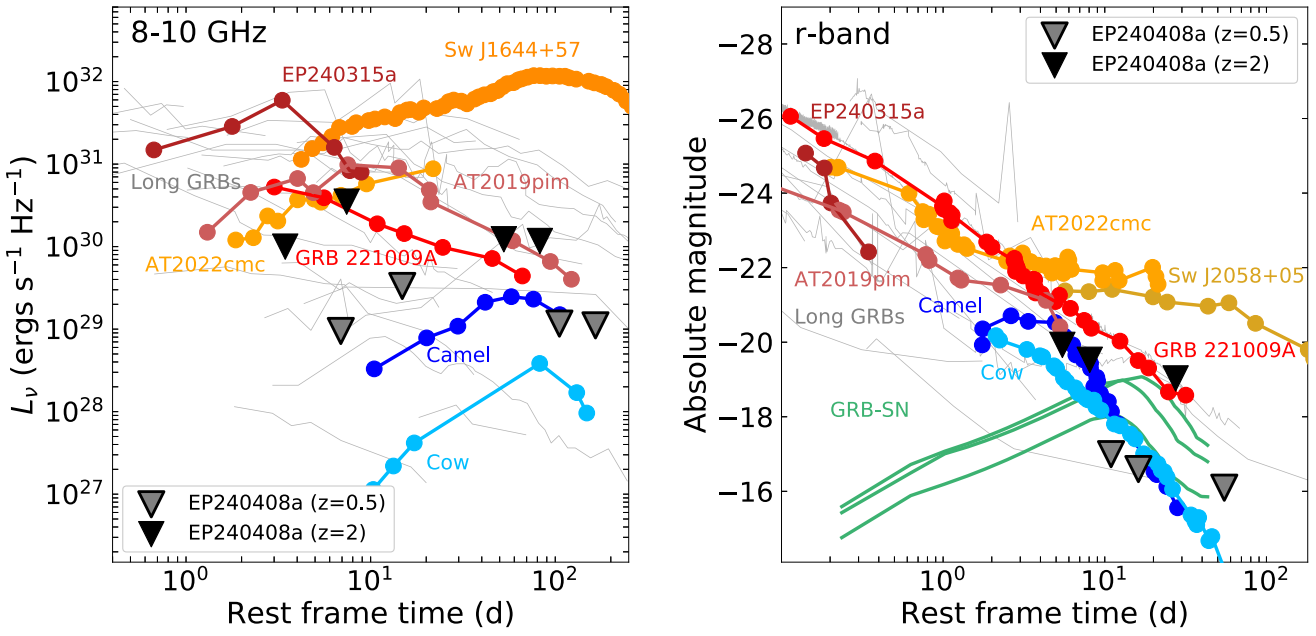

Figure 5. Left: comparison between the 10 GHz upper limits for EP240408a (downward triangles) at different assumed redshifts versus the rest frame radio luminosity of multiple classes of energetic transients, including long-duration GRBs (P. Chandra & D. A. Frail 2012; T. Laskar et al. 2022), jetted TDEs (B. A. Zauderer et al. 2011; I. Andreoni et al. 2022), and FBOTs (A. Y. Q. Ho et al. 2019; R. Margutti et al. 2019; A. Y. Q. Ho et al. 2020a; D. L. Coppejans et al. 2020). EP240315a was compiled from R. Ricci et al. (2024) and AT2019pim from D. A. Perley et al. (2024). Right: a similar comparison for observed *r*-band absolute magnitudes of various energetic transients—FBOTs (D. A. Perley et al. 2019; R. Margutti et al. 2019; D. A. Perley et al. 2021), TDEs (S. B. Cenko et al. 2012; D. R. Pasham et al. 2015; I. Andreoni et al. 2022; D. R. Pasham et al. 2023), GRB-SN (T. J. Galama et al. 1998; G. P. Srinivasaragavan et al. 2023, 2024), GRB 221009A (B. O'Connor et al. 2023), AT2019pim (D. A. Perley et al. 2024), and other GRB afterglows (M. G. Dainotti et al. 2024). The thin gray lines are long GRBs. The upper limits from our deep Gemini GMOS-S observations are shown as downward triangles at $z = 0.5$ and $z = 2$.

3.4. Disfavored Extragalactic Interpretations of EP240408a

Here, we consider a few classes of extragalactic high-energy transients that we disfavor as the progenitor of EP240408a. In Sections 3.5 and 3.6, we focus on two more likely interpretations for GRBs and TDEs, respectively.

3.4.1. Active Galactic Nuclei

The most luminous X-ray bright active galactic nuclei (AGN) have luminosities as high as $L_X = 10^{46}$ erg s^{-1} (I. Donnarumma et al. 2009; F. X. Pineau et al. 2011), and generally display X-ray variability on timescales of hours to days (P. Uttley et al. 1999, 2005). The short timescale (10 s) and high luminosity for EP240408a at $z > 0.5$ clearly disfavor the interpretation of the source as an AGN. A more distant source ($z > 0.5$) would lead to X-ray luminosities higher than the most luminous X-ray bright AGN. Moreover, the most X-ray luminous AGN also display bright optical luminosities of ≈ -28 to -30 AB mag, which would be detected by Gemini at any reasonable distance. We therefore strongly disfavor an AGN flare as the cause of EP240408a.

3.4.2. FBOT

FBOTs are characterized by a rapidly fading ($\sim$0.3 mag day^{-1}), blue ($g - r \lesssim 0.2$ mag) optical transient (e.g., M. R. Drout et al. 2014; M. Pursiainen et al. 2018) with comparable absolute magnitudes (≈ -20 mag) to superluminous supernovae. Following the discovery of AT2018cow (S. J. Prentice et al. 2018; R. Margutti et al. 2019; D. A. Perley et al. 2019), the canonical FBOT, they are now commonly identified in wide-field optical surveys. They have also been found with luminous X-ray emission (S. J. Prentice et al. 2018; R. Margutti et al. 2019; D. A. Perley et al. 2019, 2021; A. Y. Q. Ho et al. 2019, 2020b; D. L. Coppejans et al. 2020; Y. Yao et al. 2022; A. Y. Q. Ho et al. 2023). In the case of AT2018cow, the peak X-ray luminosity was $L_X = 10^{43}$ erg s^{-1} and displayed slow fading emission t^{-1} until $\sim$ 20 days (rest frame) before a sharp decay t^{-4} (R. Margutti et al. 2019). While the characteristic timescale is longer than the plateau-like emission observed from EP240408a, the behavior of a sharp break after a standard temporal decline is similar. Due to selection effects related to detecting a similar prompt X-ray transient to that identified for EP204048a, it cannot be excluded that FBOTs display similar features. Therefore, we compare the luminosity of the X-ray plateau phase of EP240408a to the peak flux of AT2018cow. EP240408a would exceed AT2018cow[49] for $z > 0.015$ ($\sim$60 Mpc), similar to the actual distance to AT2018cow, where a bright host galaxy would be visible and a large amount of dust would be required to miss a luminous cow-like optical transient in our deep, multi-epoch *riJ* images (Figure 1 and Table A2). This does not fit with the inferred intrinsic A_V from the X-ray spectrum, which at such low redshifts is almost negligible compared to the expected brightness of a typical FBOT. In fact, the strongest constraint on an FBOT-like explosion lies in the lack of bright optical emission, which implies a higher redshift ($z \gtrsim 0.5$) where the X-rays are orders of magnitude larger than from observed FBOTs. We therefore strongly disfavor an FBOT-like transient to explain EP240408a.

3.4.3. Fast X-Ray Transient

The last decade has seen the detection of a new class of X-ray transients discovered serendipitously in deep X-ray imaging, largely with Chandra and XMM-Newton (P. G. Jonker et al.

[49] Another X-ray luminous FBOT, AT2024qfm, was recently discovered with luminosity as high as 8×10^{43} erg s^{-1} (R. Margutti et al. 2024).

2013; A. Glennie et al. 2015; F. E. Bauer et al. 2017; Y. Q. Xue et al. 2019; D. Alp & J. Larsson 2020; S. Ai & B. Zhang 2021; N. Sarin et al. 2021; J. Quirola-Vásquez et al. 2022, 2023, 2024a). Referred to as fast X-ray transients (FXTs) they are characterized by short-lived (100–10,000 s) X-ray emission with typical peak X-ray luminosities in the range 10^{44-47} erg s^{-1} (H. C. I. Wichern et al. 2024). The low luminosity and short timescales of some of these events have led them to be characterized as supernova shock breakout emission (D. Alp & J. Larsson 2020) or stellar flares (A. Glennie et al. 2015), while some display similarities (such as plateaus) to short GRBs, potentially linking them to binary neutron star mergers (e.g., S. Ai & B. Zhang 2021; N. Sarin et al. 2021; D. Eappachen et al. 2023; J. Quirola-Vásquez et al. 2024a).

We note that not only are the timescales of the X-ray detections of EP240408a significantly longer than known FXTs (Figure 7), EP240408a has a peak X-ray flux two to 3 orders of magnitude higher than the brightest FXTs, which if drawn from the same population should imply a low redshift with an obvious host galaxy association. For example, CDF-S XT1 (F. E. Bauer et al. 2017) is associated with an extremely faint host galaxy in deep Hubble Space Telescope and JWST imaging with a photometric redshift of $z \approx 2.8$ (J. Quirola-Vásquez et al. 2024b). Even at this large distance, the peak X-ray luminosity is only 3×10^{47} erg s^{-1} (J. Quirola-Vásquez et al. 2024b). In contrast, already at $z \approx 0.1$ ($\sim$460 Mpc) the peak X-ray luminosity ($>10^{47}$ erg s^{-1}) of EP240408a already exceeds that of the most luminous FXTs making this interpretation unlikely.

3.5. A Peculiar GRB

GRBs are extreme transients with isotropic-equivalent energies in the range of 10^{48-55} erg. They are thought to be produced by either the merger of compact objects (B. P. Abbott et al. 2017; V. Savchenko et al. 2017; A. Goldstein et al. 2017) or the collapse of massive stars (collapsars; S. E. Woosley 1993; A. I. MacFadyen & S. E. Woosley 1999). Historically, GRBs have been separated into the classes of short versus long-duration GRBs based on the duration of their prompt gamma-ray emission with the divide at either shorter or longer than 2 s (C. Kouveliotou et al. 1993). However, there is growing evidence (e.g., GRBs 060614, 211211A, and 230307A; M. Della Valle et al. 2006; A. Gal-Yam et al. 2006; B. Yang et al. 2015; J. C. Rastinejad et al. 2022; E. Troja et al. 2022; J. Yang et al. 2022; B. P. Gompertz et al. 2023; A. Levan et al. 2024; Y.-H. Yang et al. 2024; J. H. Gillanders et al. 2023; S. Dichiara et al. 2023) that the duration separation is not a robust classifier of the GRB's progenitor. Therefore, despite the $\sim$10 s duration of the "prompt" phase of EP240408a, we do not automatically exclude the merger of two compact objects (e.g., two neutron stars) as its progenitor.

3.5.1. A "Naked" GRB

The prompt phase of GRBs is generally shortly followed by a multiwavelength "afterglow" from the forward shock produced by the interaction of the relativistic jet and the surrounding environment (P. M észáros & M. J. Rees 1997; R. Sari et al. 1998; R. A. M. J. Wijers & T. J. Galama 1999). Standard GRB afterglows at optical and X-ray wavelengths are characterized by a decay of t^{-1} followed by a t^{-2} break due to the collimation of the outflow (J. E. Rhoads 1999; R. Sari et al. 1999; D. A. Frail et al. 2001). This afterglow phase is not observed in the X-ray light curve of EP240408a, and instead we identify a plateau followed by a steep decline.

A significant fraction of both short and long GRBs also display X-ray plateaus in their early light curves, many of which are followed by extremely fast decays (even as steep as t^{-9}; E. Troja et al. 2007) that are similar to EP240408a, which shows $\delta\tau/\tau \approx 0.2$. The standard forward shock emission is incapable of decays steeper than t^{-p} (e.g., R. Sari et al. 1999), where p is the slope of the electron's power-law energy distribution, or, in the "best case scenario" $t^{-(2+\beta)} \approx t^{-3}$ if the source somehow stops emitting abruptly and only high-latitude emission is observed (P. Kumar & A. Panaitescu 2000). Therefore, plateaus followed by such steep declines, referred to as "internal plateaus" (e.g., B. Zhang et al. 2006; E. Troja et al. 2007), are generally interpreted as being due to long-lived central engine activity.

Provided the observed X-rays are due to an internal plateau, this requires that the forward shock emission from the jet must be fainter than the observed X-ray detections (Figure 3) as well as all upper limits at any wavelength. In a standard GRB interpretation, the forward shock component must exist, but in this case, it is likely extremely faint due either to a low-density (a "naked" burst, e.g., P. Kumar & A. Panaitescu 2000; D. A. Perley et al. 2009), low fraction of energy in magnetic fields ε_B (e.g., R. Barniol Duran 2014), or an early jet break (which should also impact the emission from the long-lived engine).

The lack of a known distance and the known degeneracy and broad allowed parameter range in afterglow modeling preclude a conclusive diagnostic of this possibility though experience has shown that it is generally not difficult to "hide" a forward shock, especially when applying a rarefied environment (e.g., P. Kumar & A. Panaitescu 2000; D. A. Perley et al. 2009). In what follows, we briefly test this possibility.

In the standard fireball model (e.g., P. M észáros & M. J. Rees 1997; R. A. M. J. Wijers & T. J. Galama 1999; J. Granot & R. Sari 2002), where an on-axis tophat jet propagates into an external medium $\rho_{\rm ext}(R) = A\,R^{-k}$, the forward shock emission at each time and frequency is determined by a set of six parameters: $\{z, p, E_{\rm kin}, A, \varepsilon_{\rm e}, \varepsilon_{\rm B}\}$, where p is the slope of the electron's power-law energy distribution, $E_{\rm kin}$ is the kinetic energy, and $\varepsilon_{\rm e}$ and $\varepsilon_{\rm B}$ represent the fraction of shock energy in electrons and magnetic fields, respectively. While the power-law index k determining the structure of the surrounding environment is a free parameter for simplicity, we adopt $k = 0$ for a uniform density environment and $k = 2$ for a wind-like environment (e.g., R. A. Chevalier & Z.-Y. Li 2000). These are the standard limiting cases, and we apply the analytic results of J. Granot & R. Sari (2002) in our analysis. We have assumed a post-deceleration and pre-jet-break behavior of the outflow. We neglect the effect of viewing angle, inverse Compton corrections, or reverse shock emission.

The observed synchrotron emission from the forward shock at a given time and frequency depends on the relation between the characteristic synchrotron frequencies: the self-absorption frequency $\nu_{\rm a}$, the injection frequency $\nu_{\rm m}$, and the cooling frequency $\nu_{\rm c}$. We account for Spectra 1–5 as outlined in Figure 1 of J. Granot & R. Sari (2002). We consider a range of redshifts $z = \{0.5, 1.0, 2.0\}$ and kinetic energies $E_{\rm kin} = \{10^{51}, 10^{52}, 10^{53}\}$ erg, and fix $p = 2.2$ and $\varepsilon_{\rm e} = 0.1$ for simplicity (P. Beniamini & A. J. van der Horst 2017; R. A. Duncan et al. 2023). We compute the afterglow flux at

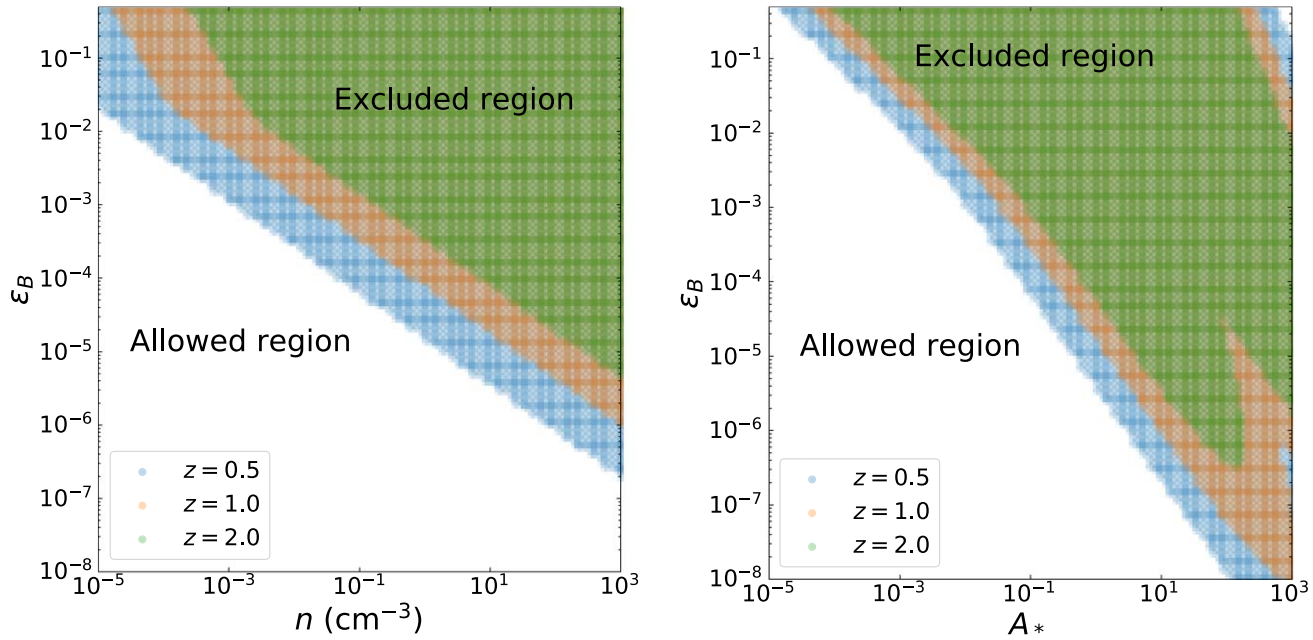

Figure 6. Left: allowed parameter space for nondetection of an afterglow in a uniform density environment ($k = 0$). Here, we have fixed $E_{\rm kin} = 10^{52}$ erg, $p = 2.2$, and $\varepsilon_e = 0.1$. Right: same as the left figure but for a wind-like environment ($k = 2$).

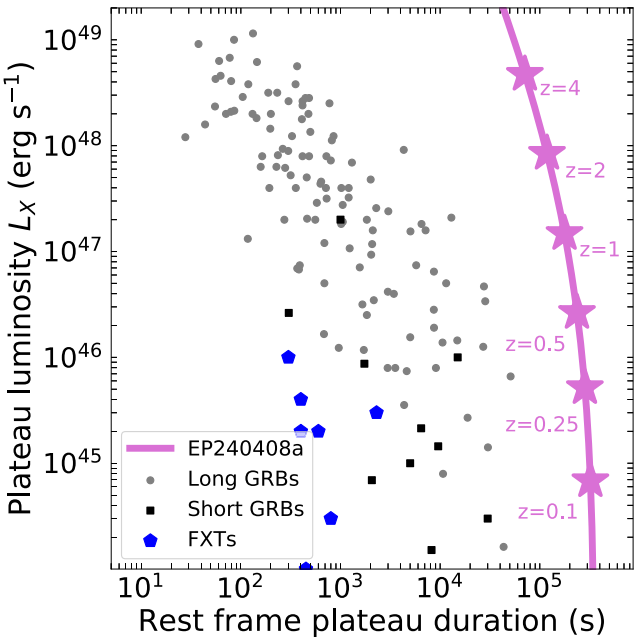

Figure 7. Observed X-ray plateau rest frame duration and luminosity for GRBs (C.-H. Tang et al. 2019; F. Xu et al. 2021) and FXTs (J. Quirola-Vásquez et al. 2024a) versus EP240408a at multiple redshifts. EP240408a does not follow the standard plateau correlations of either short or long GRBs. We note that $z \lesssim 0.5$ is strongly disfavored for EP240408a.

the time and frequency of our VLA and ATCA upper limits (10–260 days; observer frame) and include the X-ray limits from Swift (>10 days). We also use the observed X-ray detections from Swift (1.4 days) and NICER as upper limits to the forward shock emission. While we do not account for the optical and near-infrared upper limits as they can be significantly impacted by intrinsic dust in the host galaxy we do find that generally these limits are automatically satisfied. We compute the detectability over a grid of 100 log-uniform steps between $n = \{10^{-5}, 1000\}$ cm^{-3} for a uniform environment ($k = 0$), $A_* = \{10^{-5}, 1000\}$ for a wind environment ($k = 2$), and $\varepsilon_B = \{10^{-8}, 0.5\}$ for both values of k.

We emphasize that these calculations are relevant to both GRB and TDE interpretations for EP240408a (see also Section 3.6). In general, the most constraining limit is from the VLA at 10.34 days (observer frame) post-trigger, and the late-time VLA observations at 158 days and 258 days (observer frame) only exclude a small parameter space (for a wind environment) at high densities where ν_a was ~100 GHz at early times. The late-time VLA upper limits are more constraining in a TDE interpretation (see Section 3.6), as most GRBs experience a jet break before 158–258 days and we have not accounted for post-jet-break behavior in our calculations, which would lead to dim radio emission at late times.

We find that for a uniform environment, the forward shock emission is generally in the regime $\nu_a < \nu_m < \nu_c$ (Spectrum 1 from J. Granot & R. Sari 2002), whereas for a wind environment solutions are also found for $\nu_m < \nu_a < \nu_c$ (Spectrum 2 from J. Granot & R. Sari 2002). In either case (see Figure 6), the solutions require either very low-density environments or low values of ε_B. We note that values of ε_B in the range 10^{-1}–10^{-4} are generally considered standard, but have been found to be as low as 10^{-8} in some GRBs (R. Barniol Duran et al. 2013; R. Santana et al. 2014; P. Beniamini et al. 2015; B.-B. Zhang et al. 2015).

The solutions can span a larger amount of parameter space if ε_e and p are allowed to vary over a larger range of values. In general, these calculations show that we cannot completely exclude an on-axis forward shock emission from a post-deceleration jet. The allowed parameter space would be greatly expanded by allowing for off-axis viewing angles.

3.5.2. An Off-axis Jet

In Figure 7 we compare the rest frame duration and luminosity of X-ray plateaus observed from both short and long GRBs to EP240408a. EP240408a is an outlier and would

have the longest plateau ever discovered from a GRB, even longer than the class of ultralong GRBs (e.g., GRBs 060729, 101225A, 121027A, 130925A, 141121A), which are thought to have the longest lasting central engines (e.g., A. J. Levan et al. 2014; A. Cucchiara et al. 2015). However, the major difference from ultralong GRBs is the lack of energetic $\approx 10^{54-55}$ erg (isotropic-equivalent) gamma-ray emission.

The lack of gamma rays is hard, though not impossible, to explain in the context of a GRB. For example, an off-axis viewing angle would decrease the observed, line-of-sight (isotropic-equivalent) energy of the GRB, potentially allowing for consistency with the upper limits in Figure 4, which are compared to a sample of on-axis bursts. An additional, and quite relevant, impact of viewing a GRB off-axis is a likely decrease in the observed peak energy $E_{\rm p}$ toward soft X-rays (assuming $E_{\rm p}$ is constant in the comoving frame; see, e.g., T. Parsotan & D. Lazzati 2024 for a discussion of the results of numerical simulations, and F. Xu et al. 2023; H.-X. Gao et al. 2024 for discussions on the observational impact), though this will depend on the exact Lorentz factor profile of the jet. The obvious alternative is a low gamma-ray efficiency, which could be either an impact of an off-axis viewing angle (P. Beniamini & E. Nakar 2019; P. Beniamini et al. 2020b; R. Gill et al. 2020; B. O'Connor et al. 2024) or due to inefficient breakout of the jet from the progenitor star(s).

The tension between the length of the X-ray plateau of EP240408a and those of the larger sample (Figure 7) can also be reduced if EP240408a is seen off-axis. An off-axis viewing angle delays the arrival of radiation to the observer and can extend this phase (e.g., E. Nakar et al. 2002; A. Panaitescu & P. Kumar 2003; H. van Eerten et al. 2010). This would also produce less luminous X-ray emission compared to the on-axis cases shown in Figure 4 (right panel), which would likely require a very nearby event as far off-axis angles are strongly disfavored for the observed cosmological GRB sample (e.g., G. Ryan et al. 2015; T. Matsumoto et al. 2019; B. O'Connor et al. 2024).

In addition, the lack of a likely host galaxy, or even any potential low redshift host, excludes a low luminosity GRB such as GRB 060218 (A. M. Soderberg et al. 2006), which at $z = 0.033$ had a gamma-ray energy of 6×10^{49} erg and 11 hr X-ray luminosity of $L_{\rm X,11} \approx 10^{42}$ erg s^{-1}. At a similar redshift, EP204048a would have a gamma-ray energy $< 10^{48-49}$ erg and an X-ray luminosity at 11 hr of $\sim 10^{44}$ erg, quite different from even the lowest luminosity GRBs. Such low redshifts (even up to $z < 0.5$) are also excluded by the lack of detection of a coincident supernova (Figure 5, right panel) in our deep multi-epoch Gemini imaging, which probes the typical peak times of known GRB-SN (e.g., T. J. Galama et al. 1998; A. M. Soderberg et al. 2006; J. Hjorth & J. S. Bloom 2012; Z. Cano et al. 2017; G. P. Srinivasaragavan et al. 2023, 2024).

3.5.3. A Long-lived Magnetar

The most commonly adopted mechanism to explain the long-lived engine required by internal plateaus is a newborn, rapidly spinning ($P \approx$ 1–10 ms) magnetar (V. V. Usov 1992; R. C. Duncan & C. Thompson 1992) with a high magnetic field $B \approx 10^{15-16}$ G (B. Zhang et al. 2006; E. W. Liang et al. 2006; E. Troja et al. 2007; N. Lyons et al. 2010; B. D. Metzger et al. 2011; A. Rowlinson et al. 2010; A. Rowlinson et al. 2013; B. Giacomazzo & R. Perna 2013; H.-J. Lü et al. 2015; W. Chen et al. 2017). In many cases, the required magnetar approaches the maximum theoretical limits, and other interpretations for internal plateaus have been suggested (e.g., black-hole-powered photospheric emission or low Lorentz factor leading to a late deceleration of the jet) (R. Shen & C. D. Matzner 2012; P. C. Duffell & A. I. MacFadyen 2015; P. Beniamini & R. Mochkovitch 2017; P. Beniamini et al. 2017, 2020a; G. Oganesyan et al. 2020; H. Dereli-Bégué et al. 2022).

In this case of a magnetar, the plateau is produced by spin-down of the magnetar's dipole field (B. Zhang & P. Mészáros 2001)

$$L_{\rm sd} = 1.0 \times 10^{49}\, B_{15}^2 P_{-3}^{-4} R_6^6 \text{ erg s}^{-1}, \quad (1)$$

where R is the radius of the neutron star. We have adopted the convention $B_{15} = B/(10^{15}\,\text{G})$, and similar for the other parameters using cgs units. We note that the efficiency of converting the spin-down power to the observed X-ray luminosity $L_{\rm X} = \eta L_{\rm sd}$ is generally a challenge (J. Granot et al. 2015; P. Beniamini & R. Mochkovitch 2017). The end of the plateau phase is typically taken to be the spin-down timescale of the magnetar (B. Zhang & P. Mészáros 2001)

$$t_{\rm sd} = 2.0 \times 10^3\, I_{45}\, B_{15}^{-2} P_{-3}^2 R_6^{-6} \text{ s}, \quad (2)$$

where I is the moment of inertia of the neutron star. The temporal decay following the spin-down time is (P. Beniamini & R. Mochkovitch 2017)

$$L = L_{\rm sd}\left(1 + \frac{n-1}{2}\frac{t-t_{\rm o}}{t_{\rm sd}}\right)^{\frac{1+n}{1-n}}, \quad (3)$$

where $t_{\rm o}$ is the start of the spin-down, and n is the magnetic braking index, which for $n = 3$ yields the standard $\propto t^{-2}$ decay. A t^{-7} decay as observed for EP240408a requires $n \approx 1.33$, consistent with that inferred for some isolate pulsars (O. Hamil et al. 2015). In addition, the temporal decline can steepen if the magnetar collapses to a black hole, but this would limit the allowed energy reservoir, which considering the estimate $P \sim 1$ ms, is already constraining.

Despite the long-lasting plateau ($\sim 3.5 \times 10^5$ s), we find a suitable match to the required luminosity and duration for a magnetar with $B \approx 10^{14}$ G and $P \approx 1$ ms, assuming $z \approx 1$. These solutions are degenerate with redshift and radiative efficiency, and thus, we only provide a single example. In any case, the initial spin period of the neutron star would have to be close to the breakup limit (J. M. Lattimer & M. Prakash 2004). These values, in particular the magnetic field, are slight outliers when compared to those inferred for either short ($B \approx 10^{16}$ G; A. Rowlinson et al. 2010; A. Rowlinson et al. 2013; B. P. Gompertz et al. 2014; H.-J. Lü et al. 2015) or long GRBs ($B \approx 10^{15}$ G; N. Lyons et al. 2010; S. X. Yi et al. 2014) and fall closer to SLSN ($B \approx 10^{13-14}$ G; M. Nicholl et al. 2017). This is not surprising given the longer plateau duration $t_{\rm sd} \propto B^{-2}$, which requires a smaller magnetic field.

3.5.4. A Dissipative Photosphere

There are other possible explanations for the observed plateau other than a long-lived magnetar or an off-axis jet. A black hole engine was proposed for GRB 070110 (P. Beniamini & R. Mochkovitch 2017), whereas the central engine launches a second lower Lorentz factor outflow, which produces

photospheric emission (P. Beniamini & P. Kumar 2016), leading to the observed plateau. We note, however, that this model is independent of the class of central engine, which simply provides an energy source that must then be transformed (e.g., a dissipative photosphere) into the observed radiation. P. Beniamini & R. Mochkovitch (2017) considered a jet that efficiently dissipates energy below the photosphere, leading to a thermal Comptonized X-ray spectrum with peak energy $E_{\rm p,X} \lesssim 0.5$–1 keV. In the observed 0.3–10 keV bandpass such a spectrum would appear as $F_\nu \approx \nu^{-1}$ (similar to EP240408a). However, in the case of EP240408a, the peak energy is ∼4 keV (Figure 2).

Applying the model from P. Beniamini & R. Mochkovitch (2017), we can derive the Lorentz factor Γ at the photosphere required to produce the observed X-ray plateau luminosity $L_{\rm th}$ as

$$\Gamma = 15\frac{\lambda^{1/2}}{\epsilon_{\rm rad,-2}^{1/4}}(1+\sigma)^{-1/4}L_{\rm th,47}^{1/8}E_{\rm p,X}^{1/2}, \quad (4)$$

where λ is an order unity factor determined by the exact emission spectrum,[50] $\epsilon_{\rm rad}$ is approximately the efficiency of a nondissipative photosphere, and $(1+\sigma)$ is the magnetization parameter. In this model, we find that the observations of EP240408a could be roughly reproduced by a photosphere with Lorentz factor $\Gamma \approx 30$.

As discussed in P. Beniamini & R. Mochkovitch (2017), the Lorentz factor is not severely impacted by the allowed ranges of λ, $\epsilon_{\rm rad}$, or $(1+\sigma)$. These parameters instead have a larger impact on the (observer frame) geometric timescale (P. Beniamini & R. Mochkovitch 2017)

$$t_{\rm geo} = 0.25\frac{1+z}{2}\frac{\epsilon_{\rm rad,-2}(1+\sigma)^{1/4}}{\lambda^{5/2}}\frac{L_{\rm th,47}^{3/8}}{E_{\rm p,X}^{5/2}}\ {\rm s}. \quad (5)$$

However, the geometric timescale is always significantly shorter than the plateaus decay timescale, which strongly suggests that the rapid t^{-7} decay is due to the cessation of the central engine.

3.6. A High-redshift Jetted TDE

The population of relativistic jetted TDEs is small, with only four candidates (J. S. Bloom et al. 2011; A. J. Levan et al. 2011; B. A. Zauderer et al. 2011; D. N. Burrows et al. 2011; S. B. Cenko et al. 2012; G. C. Brown et al. 2015; D. R. Pasham et al. 2015; I. Andreoni et al. 2022; D. R. Pasham et al. 2023) uncovered since their initial discovery in 2011 (J. S. Bloom et al. 2011; A. J. Levan et al. 2011; D. N. Burrows et al. 2011). They are produced by the tidal shredding of a stellar mass star by a massive black hole ($M_{\rm BH} \approx 10^{5-8}M_\odot$). These TDEs are generally characterized by luminous X-ray and radio emission (Figures 3 and 5). At X-ray wavelengths, they display rapid short-term variability (approximately hours) on top of a power-law decay of $\approx t^{-2}$.

Only Sw J1644+57 ($z = 0.35$) was detected by a gamma-ray satellite (Swift/BAT; J. R. Cummings et al. 2011) in flight, as opposed to a ground analysis. Even then, Sw J1644+57 was identified through am ∼1000 s long image trigger (J. R. Cummings et al. 2011; T. Sakamoto et al. 2011b; A. J. Levan et al. 2011) and not bright enough to trigger Swift/BAT as a normal GRB. Accompanying its multiple gamma-ray triggers, Sw J1644+57 exhibited exceptional soft X-ray (0.3 − 10 keV) radiation with peak luminosity $L_{\rm X} \approx 3 \times 10^{48}$ erg s^{-1} and an average luminosity over 10^6 s of 9×10^{46} erg s^{-1} (J. S. Bloom et al. 2011). We note that the observed peak X-ray flux of the initial trigger of EP240408a is a factor of ∼ 10 higher than the brightest soft X-ray detection of Sw J1644+57.

Two additional jetted TDEs, Sw J2058+05 at $z = 1.19$ (S. B. Cenko et al. 2012) and Sw J1112-82 at $z = 0.89$ (G. C. Brown et al. 2015), were both identified in an automated ground-based analysis by the Swift/BAT Hard X-ray Transient Monitor (H. A. Krimm et al. 2013) in 4 day binned windows (15−50 keV). As such, their gamma-ray variability or spectra could not be measured, and they cannot be obviously compared to the population of GRBs in Figure 4.

In contrast to the other three jetted TDEs, AT2022cmc was discovered as a rapidly fading optical transient and was not detected in gamma rays ($z = 1.19$; I. Andreoni et al. 2022; D. R. Pasham et al. 2023; L. Rhodes et al. 2023; Y. Yao et al. 2024). I. Andreoni et al. (2022) estimated a <5% chance of Swift/BAT detecting similar gamma-ray flares to those observed from Sw J1644+57 at redshift $z = 1.19$. Due to its larger distance, AT2022cmc remains hostless to depth 24.5 AB mag (I. Andreoni et al. 2022). In the case of AT2022cmc, despite the subarcsecond localization, the lack of an underlying host precluded the determination as to whether it was truly a nuclear transient. In the case of EP240408a, the lack of subarcsecond localization (Figure 1) is the limiting factor, and the slight offset from the XRT-enhanced position similarly does not rule out EP240408a as a nuclear transient.

Therefore, we find that the lack of gamma rays does not immediately disfavor a jetted TDE interpretation, nor does the prompt soft X-ray detection. If indeed the X-rays can shut off on timescales of ∼4 days, there is a strong bias against finding such fast X-ray transients. In fact, there are selection biases that exist, especially prior to the launch of EP (W. Yuan et al. 2015, 2022), toward detecting similar prompt X-ray transients to EP240408a (J. W. Hu et al. 2024a) or relativistic jetted TDEs in general.

3.6.1. The Nature of the X-Ray Emission

While the X-ray radiation observed from EP240408a can match the luminosity of known relativistic jetted TDEs (Figure 3) at $z \approx 1$–2, the observed timescales are significantly shorter (Figure 3). While after ∼10 days, Sw J1644+57 transitioned to an approximately $t^{-5/3}$ decay (D. N. Burrows et al. 2011; J. S. Bloom et al. 2011), EP240408a appears to potentially shut off with an extremely fast decay ($\delta\tau/\tau \approx 0.2$). In particular, central engine cessation of other jetted TDEs is on the order of hundreds of days (100–400 days in the rest frame) (V. Mangano et al. 2016; A. J. Levan et al. 2016; T. Eftekhari et al. 2018, 2024), whereas a sharp decline is observed in EP240408a after only ≲4 days when considering the impact of redshift. It is unclear whether this is natural variability in X-rays, like the sharp variability observed at early times for Sw J1644+57 (Figure 3), at high-z that then fades below NICER, Swift, and NuSTAR sensitivity.

For starters, if we assume a typical black hole mass for the observed relativistic jetted TDEs $M_{\rm BH} \approx 10^{6-8}M_\odot$, the Eddington luminosity is in the range 10^{44-46} erg s^{-1}. Even ignoring the initial EP trigger, the X-ray plateau luminosity implies a highly super-Eddington outflow with Eddington ratio $\lambda \approx$ 5–500 (20–2000) at $z \approx 1.0$ (2.0). This may favor

[50] The parameter λ is 1 for a pure non-Comptonized photosphere and less than 1 for a Comptonized photosphere.

redshifts more similar to AT2022cmc at $z = 1.19$ as the Eddington ratio at $z \gtrsim 2$ is quite extreme. We note that the initial EP trigger is ~500 times brighter and would require extreme super-Eddington accretion. For reference, Sw J1644+57 exhibited an Eddington ratio (beaming corrected) of only ~1200 (P. Beniamini et al. 2023).

If we assume the emission comes from a highly collimated, relativistic jet (similar to Sw J1644+57), it significantly decreases the required energy budget. For instance, the beaming factor of a tophat jet is $f_b \approx \theta_c^2/2$, where θ_c is the jet's core half-opening angle. Adopting a typical opening angle of $\theta_c = 0.1$ rad yields a beaming correction of $f_b^{-1} \approx 200$. Applying this to the initial flare detection of EP240408a leads to an Eddington ratio of between $\lambda_{\rm peak} \approx 13$ and 1250 (50–5000) at $z \approx 1.0$ (2.0). These ratios can be decreased further if the opening angle of the jet is smaller than 0.1 rad (6 deg). This implies the observed X-ray emission requires a relativistic jet (with likely a small viewing angle) and that we are observing X-rays from an internal dissipation process (due to the short variability timescales observed for the plateau).

3.6.2. Fallback Timescale

The end of the plateau can be associated with the fallback timescale of the disrupted stellar material (e.g., D. N. Burrows et al. 2011; J. S. Bloom et al. 2011; S. B. Cenko et al. 2012) from a main-sequence star in which case the fallback accretion rate begins to decay as $\approx t^{-\alpha}$, where $\alpha = 5/3$ (complete disruption) or 2.2 (partial disruption) is generally adopted (J. Guillochon & E. Ramirez-Ruiz 2013). The fallback time is given by (A. Ulmer 1999; N. Stone et al. 2013; N. C. Stone & B. D. Metzger 2016)

$$t_{\rm fb} = 3.5 \times 10^5 \ {\rm s} \left(\frac{M_{\rm BH}}{10^4 M_\odot}\right)^{1/2} \left(\frac{M_*}{M_\odot}\right)^{-1} \left(\frac{r_*}{R_\odot}\right)^{3/2}, \quad (6)$$

where we can further adopt $r_* = M_*^{0.8}$ for a main-sequence star (N. Stone et al. 2013; N. C. Stone & B. D. Metzger 2016). Thus, we either require an intermediate-mass black hole or a subsolar-mass star. The disruption of a subsolar mass star is plausible based on the standard initial mass function (G. Chabrier 2003). The Eddington ratio scales as $\lambda \propto M_{\rm BH}^{-3/2}$ and thus smaller black holes are capable of higher accretion rates, leading to greater super-Eddington luminosities.

An alternative possibility is the disruption of a white dwarf by a black hole (e.g., C. S. Ye et al. 2023)

$$t_{\rm fb} = 1.0 \times 10^5 \ {\rm s} \left(\frac{M_{\rm BH}}{10^7 M_\odot}\right)^{1/2} \left(\frac{M_{\rm WD}}{0.6 M_\odot}\right)^{-1} \left(\frac{r_{\rm WD}}{10^9 \ {\rm cm}}\right)^{3/2}, \quad (7)$$

where we apply the white dwarf mass–radius relation following M. Nauenberg (1972). In this case, in order to achieve a late enough fallback timescale requires a larger black hole. A similar value of 10^5 s is derived for $M_{\rm BH} \approx 10^6 M_\odot$ and $M_{\rm WD} \approx 0.3 M_\odot$.

3.6.3. Transition from Super-Eddington to Sub-Eddington Accretion

An alternative is the cessation of the central engine, which can be interpreted at the transition from super-Eddington accretion to sub-Eddington accretion (e.g., B. A. Zauderer et al. 2013; D. R. Pasham et al. 2015; T. Eftekhari et al. 2024). This can be taken as the shutoff of a relativistic jet. This occurs at an Eddington ratio λ of unity ($\lambda = 1$), such that (T. Eftekhari et al. 2024)

$$M_{\rm BH} = 8.4 \times 10^6 \ L_{\rm jet,off,47} \left(\frac{\varepsilon_{\rm disk,-1}}{\varepsilon_{\rm jet,-1}}\right) \left(\frac{f_{\rm b}}{200}\right) f_{\rm bol,3} \ M_\odot, \quad (8)$$

where $\varepsilon_{\rm disk}$ and $\varepsilon_{\rm jet}$ represent the radiative efficiencies of the disk and jet, respectively. T. Eftekhari et al. (2024) finds that the $\varepsilon_{\rm jet}/\varepsilon_{\rm disk} \gtrsim 0.1$. We convert the isotropic equivalent luminosity of the jet to the intrinsic luminosity using a tophat jet beaming factor $f_{\rm b} = (1 - \cos\theta_c) \approx \theta_c^2/2$. As before, we adopt a jet half-opening angle $\theta_c = 0.1$ rad such that $f_{\rm b}^{-1} = 200$. An additional bolometric correction to the jet energy is $f_{\rm bol} = 3 f_{\rm bol,3}$ is also made (T. Eftekhari et al. 2024).

Following T. Eftekhari et al. (2024), the time of the transition to sub-Eddington accretion occurs at

$$t_{\rm off} = t_{\rm fb} \lambda_{\rm p}^{1/\alpha}, \quad (9)$$

where $\lambda_{\rm p}$ is the peak Eddington ratio (N. Stone et al. 2013; N. C. Stone & B. D. Metzger 2016)

$$\lambda_{\rm p} = 133 \ f_{\rm in} \ \varepsilon_{\rm disk,-1} M_{\rm BH,6}^{-3/2} \left(\frac{M_*}{M_\odot}\right)^2 \left[\frac{3(\alpha-1)}{2}\right], \quad (10)$$

where $f_{\rm in}$ accounts for multiple efficiencies related to the fallback process (see T. Eftekhari et al. 2024 for further discussion).

This interpretation immediately requires a short fallback time, which can potentially be accommodated by the disruption of a white dwarf by an intermediate-mass black hole Equation (7). For consistency with Equation (8), this in turn likely also requires either a smaller redshift or a significantly narrower jet, both of which lead to a lower jet luminosity and smaller required black hole mass. Assuming the disruption of a $0.6 M_\odot$ white dwarf by an intermediate-mass black hole $\approx 10^5 M_\odot$, as favored by T. Eftekhari et al. (2024) to explain other jetted TDEs, yields $t_{\rm fb} \approx 10^4$ s and a shutoff time of $t_{\rm off} \approx 2.7 \times 10^5$ s for $\alpha = 2.2$. Given the multiple uncertainties related to the efficiency of the fallback process, it is possible to shorten this timescale further, allowing it to match the rest frame shutoff time, $3.5 \times 10^5/(1+z)$ s, of EP240408a over a variety of redshifts.

One possibility to reduce these constraints is that the initial EP trigger is related to the peak of the fallback accretion rate and that the initial disruption of the star occurred on earlier timescales. However, an earlier disruption time immediately implies that the temporal slopes determined in this work are shallower than reality, and that the break decay must be steeper than t^{-7}, which is already challenging to explain. We note that this can allow for the initial slope, prior to the steep decline, to match either $t^{-5/3}$ or $t^{-2.2}$ (for explosion times between ~ 3 and 10 days prior to the EP trigger). The major issue with this interpretation lies in explaining the factor of ~ 1000 × the flare of the EP trigger if it occurs a few days after disruption. Such a flare has not been previously observed in any other jetted TDE.

An alternative scenario proposed by O. Teboul & B. D. Metzger (2023) suggests that early precession of the jet may have delayed its breakout from the surrounding ejecta. The breakout time for a precessing jet can be on the order of a few days to tens of days (O. Teboul & B. D. Metzger 2023), increasing the jet shutoff time to more reasonable values, and decreasing the strong constraints on the progenitor system (e.g., black hole mass). This model also explains the lack of early short-term variability, suggesting that the

rapid X-ray brightness variations from Sw J1644+57 were due to an early jet breakout while the jet was still precessing across the line of sight (Figure 3), whereas jet breakout after alignment with the black hole's spin leads to a smooth decay of the X-ray light curve as observed from AT2022cmc and EP240408a.

3.6.4. Delayed Radio Emission

Due to the lack of radio emission detected for EP240408a (Figure 5) and the short variability timescales ($\delta\tau/\tau \approx 0.2$), we interpret the X-rays as arising from an internal process within the jet. The lack of optical emission (Figure 5) can be due to intrinsic extinction in the host galaxy, as was the case for Sw J1644+57. The expected A_V from the inferred X-ray hydrogen column density (Section 2.12) is 1.4 (6.3) mag (T. Güver & F. Özel 2009) at $z \approx 0.5$ (2.0), and can easily lead to a nondetection at higher redshifts. Harder to explain is the lack of bright radio in our sensitive multi-epoch VLA and ATCA observations. It is possible that these observations occur too early (i.e., pre-deceleration) and that eventually rising radio emission could become detectable, or that the self-absorption frequency is above our observations at 5−18 GHz out to $\sim$ 260 days (observer frame).

Delayed radio emission has been uncovered in a variety of TDEs (A. Horesh et al. 2021a, 2021b; E. S. Perlman et al. 2022; I. Sfaradi et al. 2022; Y. Cendes et al. 2022, 2024) on timescales of $>$ 100–1000 d. This delayed radio emission has been interpreted either as either late jet launching from a long-lived central engine (S. van Velzen et al. 2016; A. Horesh et al. 2021a; Y. Cendes et al. 2022, 2024), an off-axis relativistic jet with Lorentz factor on the order of tens (T. Matsumoto & T. Piran 2023; P. Beniamini et al. 2023; I. Sfaradi et al. 2024), or delayed breakout due early jet precession (O. Teboul & B. D. Metzger 2023). The further off-axis the viewing angle, the later the time of the peak and the steeper the temporal slope of the rising emission (e.g., AT2018hyz with a t^6 rise around 1000 days after discovery; Y. Cendes et al. 2022; I. Sfaradi et al. 2024). Due to the inferred range of Eddington ratios, it is likely that the jet of EP240408a cannot be very far off-axis. In addition, the alternative explanation that is typically invoked requires an outflow launched at late times (e.g., Y. Cendes et al. 2022, 2024), which conflicts with the already existing jet inferred from the X-rays.

As the jet is unlikely to be very far off-axis, we conclude that this is an unlikely reason for delaying the radio emission and that instead plausible interpretations include synchrotron self-absorption or late jet deceleration due to a low initial Lorentz factor $\Gamma \lesssim 10$. We note that an equipartition analysis (R. Barniol Duran et al. 2013; R. Barniol Duran & T. Piran 2013; T. Matsumoto & T. Piran 2023) is not constraining as we have no robust limit on either the peak frequency $\nu_{\rm peak}$ or the peak flux $F_{\nu,\rm peak}$. Instead, we simply compute the synchrotron emission from a forward shock propagating into an external medium $\rho_{\rm ext}(R) = A(R/R_0)^{-k}$ for a range of parameters (J. Granot & R. Sari 2002). We focus for simplicity on the limiting cases of $k = 0$ for a uniform density environment and $k = 2$ for a wind-like environment, though the exact index does not have to be either. The nondetection of forward shock emission requires low external densities or small fractions of energy in magnetic fields, as previously noted in Section 3.5 and Figure 6. These solutions are not impossible for a TDE jet and we therefore cannot rule out a post-deceleration forward shock. An initially high synchrotron self-absorption ($>$100 GHz) frequency allows for nondetection of radio emission in a wind environment for large densities (Figure 6, right panel), but requires a significant amount of dust to not be detected in the optical. This solution would predict luminous radio emission at higher frequencies or at the same frequencies at later times and is mainly ruled out by the late-time VLA upper limits (158 days and 258 d; observer frame). This high-density solution disappears for higher kinetic energies (e.g., 10^{53} erg) or lower redshifts (e.g., $z < 0.5$). Therefore, only for a wind-like environment with high densities $A_* > 100$ and $E_{\rm kin} < 10^{53}$ erg do we predict detectable radio emission at later times or higher frequencies.

While these calculations (Figure 6) assume that the jet is already in a post-deceleration phase, this may not be the case for a TDE jet. Thus, we also consider the possibility that the jet has a low Lorentz factor and has not decelerated until $>$260 days (observer frame). In this case, the peak of the afterglow has not occurred and the emission is rising with time. This analysis mainly refers to a TDE interpretation, but could be relevant to GRBs in relation to low Lorentz factor dirty fireballs. We consider here the case of an on-axis jet, but note that off-axis viewing angles will delay the observed deceleration time further (e.g., E. Nakar et al. 2002; B. O'Connor et al. 2024). The (on-axis) deceleration time (observer frame) of an ultrarelativistic outflow with initial Lorentz factor Γ is given by (R. Sari & T. Piran 1999; E. Molinari et al. 2007; G. Ghisellini et al. 2010; G. Ghirlanda et al. 2012; L. Nava et al. 2013; F. Nappo et al. 2014; G. Ghirlanda et al. 2018)

$$t_{\rm dec} = \begin{cases} 6.4\,(\frac{1+z}{2})\Gamma_1^{-8/3}\,E_{\rm kin,53}^{1/3}\,n_{-1}^{-1/3}\ \text{days}, & k=0, \\ 15.2\,(\frac{1+z}{2})\Gamma_1^{-4}\,E_{\rm kin,53}\,A_{*,-1}^{-1}\ \text{days}, & k=2, \end{cases} \tag{11}$$

with $k = 0$ for a uniform density n environment, and $k = 2$ and A_* representing a wind-like environment (e.g., R. A. Chevalier & Z.-Y. Li 2000). In Figure 8, we show the allowed parameter space in terms of the Lorentz factor and kinetic energy for both a uniform interstellar medium (ISM) and wind environment. The allowed range of space, which also depends on density and (marginally) redshift, favors low Lorentz factor outflows with $\Gamma \lesssim 10$ for either environment when considering reasonable densities.

If the jet is not ultrarelativistic, instead the deceleration time (for a uniform density environment) can be estimated as (E. Nakar & T. Piran 2011)

$$t_{\rm dec,s} \approx 600\left(\frac{1+z}{2}\right)E_{\rm kin,52}^{1/3}n^{-1/3}\beta^{-5/3}\ \text{days}, \tag{12}$$

where $c\beta$ is the initial velocity of the outflow. For a reasonable range of energies and densities, the deceleration in this regime can be significantly larger than 260 d, especially if $\beta \ll 1$ (see Figure 8). This is also the case for a wind environment. In either situation, the allowed range of β is completely unconstrained below $\beta < 0.9$ for kinetic energies as low as 10^{51} erg.

Therefore, there are multiple plausible interpretations for the lack of radio detections in our VLA and ATCA observations. Thus, we predict that luminous radio emission may become detectable from EP240408a on the timescale of a few hundred days (e.g., AT2018hyz), similar to other TDEs. The detection of late-time radio emission would exclude a GRB interpretation.

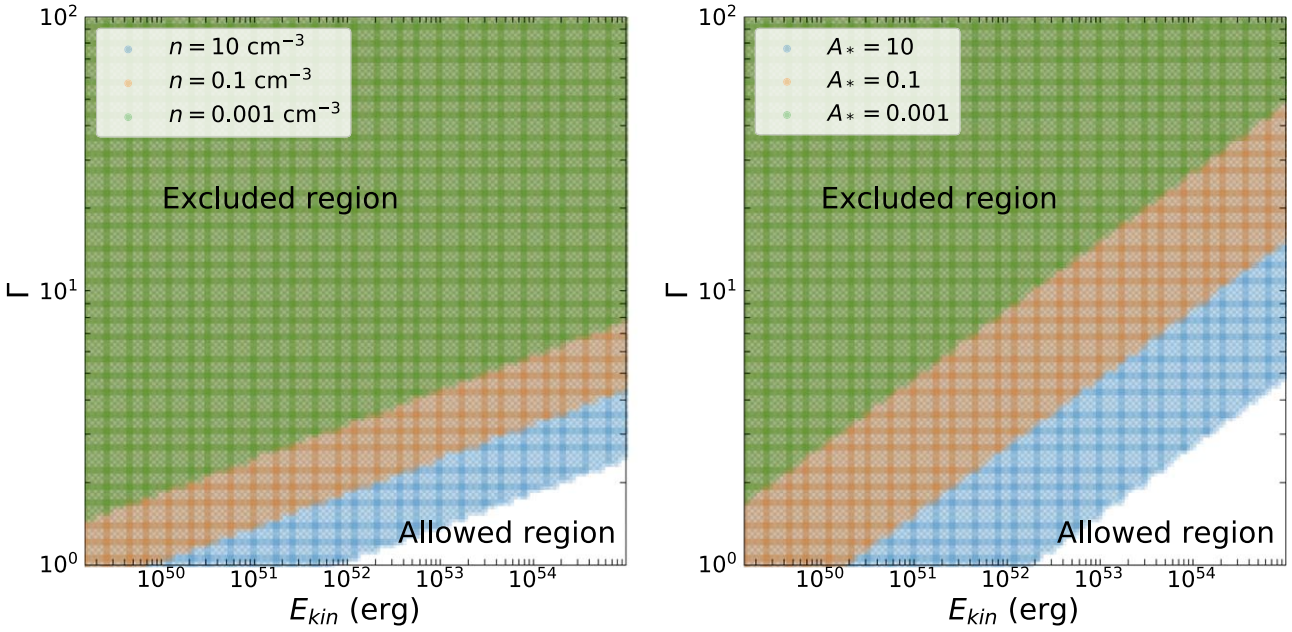

Figure 8. Left: allowed parameter space in Lorentz factor Γ and isotropic-equivalent kinetic energy for delayed jet deceleration of an ultrarelativistic outflow to after $> 158 - 258$ days (observer frame) in a uniform density environment ($k = 0$). Here, we have fixed $z = 1$ due to the larger dependence and allowed range of the other parameters. Right: same as the left figure but for a wind-like environment ($k = 2$).

Further late-time radio observations can aid in determining the nature of EP240408a.

3.7. Interpretation of the Spectral Break

Using the X-ray data obtained by NICER, we are able to model the time-resolved X-ray spectra (Section 2.12.2) with an absorbed broken power law and measure a time-varying spectral break between 3 and 6 keV (observer frame) as detailed in Figure 2. The exact time evolution of the spectral break is not well constrained due to declining data quality as the source fades, but it does not appear in the earliest NICER data. As shown in Figure 2 (bottom panels), the first appearance of the spectral break is in the third epoch (E3) of NICER data at $\sim$ 3.4 days (observer frame). The spectral break energy appears relatively fixed in energy within errors, and does not display drastic changes between epochs. The median value is around $E_{\rm break} \approx 4.5$ keV (observer frame).

Spectral breaks are a common feature of synchrotron radiation (J. Granot & R. Sari 2002) and can be due to the passage of a few characteristic frequencies through the observed band. These breaks are commonly observed in GRBs, and also in some relativistic jetted TDEs (e.g., AT2022cmc) (Y. Yao et al. 2024). Synchrotron radiation can arise from both internal and external processes to the jet. In an external shock origin, the characteristic synchrotron frequencies, such as the cooling frequency $\nu_{\rm c}$ and the peak frequency $\nu_{\rm m}$ have a well-known temporal dependence (J. Granot & R. Sari 2002) that has also been measured in GRB afterglows. The time dependence of the cooling frequency is modified depending on the external environment with $\nu_{\rm c} \propto t^{-1/2}$ for a uniform medium and $\nu_{\rm c} \propto t^{0.5}$ for a wind-like medium, neglecting inverse Compton corrections (R. Sari & A. A. Esin 2001; Y.-C. Zou et al. 2009; P. Beniamini et al. 2015). Instead, the peak frequency $\nu_{\rm m}$ does not depend on the surrounding environment $\nu_{\rm m} \propto t^{-3/2}$. However, a declining spectral break is disfavored by our analysis, especially one with such a strong time evolution.

While the exact evolution of the spectral break observed in EP240408a is uncertain, it tends to be roughly consistent with a $t^{0.5}$ within errors (and we note the time dependence can be modified if the value of k deviates from $k = 2$). This is mainly due to the fact that the break energy is most well constrained at $\sim$3.4 d, and seems to increase following this based on the agreement between the values measured in the latter epochs (E5 to E8; Figure 2). In this case, it may well be due to the increase of the cooling frequency in a wind-like environment. However, it must be noted that the observed change in the spectral index of the broken power law above and below the spectral break is on the order of 0.5–1.0, whereas the change in slope due to the passage of the cooling frequency should be 0.5. In addition, the light curve does not follow the expected temporal behavior of an external shock synchrotron afterglow, especially due to the very steep decay at later times.

Instead, the observed X-ray emission may be due to nonthermal radiation from processes internal to the jet (such as internal shocks) at small radii (as required due to the extremely steep decay). If we assume the Lorentz factor of the emitting material is constant and adopt that the radius goes as $R \sim \Gamma^2 t$, we can estimate that $\nu_{\rm c} \propto R^{(3/2)k-2} \propto t^{(3/2)k-2}$, which decreases for a uniform medium and increases for a wind-like medium, as in the external shocks scenario but with a steeper time dependence in both cases (J. Granot & R. Sari 2002). As k does not have to exactly satisfy either assumed density profile, the time evolution of $\nu_{\rm c}$ can easily span a wide range and be consistent with our observations of the spectral break.

We note that a spectral break between 10 and 15 keV was observed in the relativistic TDE AT2022cmc (Y. Yao et al. 2024). The temporal dependence there was roughly consistent with $\nu_{\rm c} \propto t^{0.5}$ between 7.8 and 17.6 days (observer frame). This evolution could not be confirmed in the third epoch at 36.2 d, potentially due to the decreased data quality at this later time.

While the spectral break is most easily explained in a synchrotron emission model, and in general we favor a relativistic jetted TDE explanation for EP240408a, it is also possible to explain in the models proposed for the X-ray plateau in a GRB interpretation. For example, in the dissipative photosphere model (Section 3.5.4), a fixed spectral break easily matches the model prediction. As the geometric timescale Equation (5) is significantly shorter than the observed decay timescale, any variability, even of the spectral break, is directly impacted by the central engine activity and is therefore hard to completely exclude due to the wide range of possibilities for the engine's behavior (even from observations of GRBs). In the dissipative photosphere model, a time-varying spectral break $E_{\rm p} \propto (1+\sigma)^{1/2}\varepsilon_{\rm rad}^{1/2}\Gamma^2$ could be potentially explained by a time evolution of the magnetization σ, radiation efficiency $\varepsilon_{\rm rad}$, or outflow Lorentz factor Γ. However, envisioning a time evolution of these parameters that leads to an increasing break energy $E_{\rm p}$ is less clear and may disfavor this interpretation for the plateau.

3.8. Comparison of Intrinsic Rates

We compare the intrinsic rate of long GRBs and jetted TDEs. The inferred local rate of long GRBs is 79^{+57}_{-33} Gpc^{-3} yr^{-1} (G. Ghirlanda & R. Salvaterra 2022) with a redshift evolution of $(1+z)^{3.2}$ out to $z \approx 3$. Jetted TDE rates are more uncertain due to their smaller population and range between $\sim$ 0.3 and 20 Gpc^{-3} yr^{-1} for Sw J1644+57 and AT2018hyz, respectively (T. Piran & P. Beniamini 2023). We adopt the intrinsic rate of the jetted TDE AT2018hyz at $z = 0.0457$ (Y. Cendes et al. 2022; T. Piran & P. Beniamini 2023; I. Sfaradi et al. 2024), which is the closest and therefore leads to a higher (beaming corrected) rate of $\sim$ 20 Gpc^{-3} yr^{-1}. This is consistent at the 2σ level with the rate of long GRBs at a similar redshift (G. Ghirlanda & R. Salvaterra 2022). The inferred rate of AT2018hyz would be significantly higher if interpreted as an on-axis jet (Y. Cendes et al. 2022), not to mention the significant selection effects against detecting a similar event. This comparison implies that both jetted TDEs and long GRBs may occur at similar rates in the local universe. However, EP240408a likely occurred at significantly higher redshifts $z \approx 1-2$ in which case the intrinsic long GRB rate is higher by a factor of $\sim$10–30, whereas the rate of TDEs likely decreases rapidly (C. S. Kochanek 2016).

4. Conclusions

In this work we have presented the results of our extensive multiwavelength (X-ray, ultraviolet, optical, near-infrared, and radio) follow-up campaign of the *EP* transient EP240408a. Our campaign, which includes deep Gemini observations, uncovered a possible host galaxy association. However, the faint nature of the host leaves the distance scale and luminosity of EP240408a unconstrained. Based on the host brightness, we favor higher redshifts ($z \gtrsim 0.5$) where the peak X-ray luminosity exceeds 10^{49} erg s^{-1}. We note, however, that the lack of subarcsecond localization precludes both an accurate diagnostic of the host association or the possibility that the candidate uncovered by Gemini is potentially an unrelated foreground galaxy.

The observed properties of EP240408a, such as the long-lived duration ($\sim$ 5 d), (likely) high X-ray luminosity, and lack of bright radio emission, do not directly align with any known transient class at any likely redshift. We have considered a variety of interpretations for the multiwavelength data set, and favor a peculiar GRB or jetted TDE at high-z ($z \gtrsim 1$), though neither perfectly explains the observations. The distinguishing factor between these two scenarios will be the detection or nondetection of radio emission on the timescale of hundreds of days. In addition, measuring the distance scale (redshift) of the candidate host galaxy, which may require space-based observations (e.g., Hubble Space Telescope or James Webb Space Telescope), is critical to the interpretation of EP240408a. Future follow-up of EP transients on rapid timescales may reveal more events falling into this rare, and potentially new, class of transient and aid in determining its true nature.

Acknowledgments

The authors thank the EP team, in particular Nanda Rea, Weimin Yuan, Wenda Zhang, and Chichuan Jin, for useful discussions. The authors acknowledge Jimmy DeLaunay regarding Swift/BAT and Fermi/GBM, Gaurav Waratkar regarding *AstroSat*/CZTI, and Dmitry Svinkin regarding Konus-Wind. B. O. acknowledges useful discussions with Phil Evans regarding the XRT data, Kathleen Labrie regarding the Gemini data, and Gourav Khullar and Anna O'Grady regarding the interpretation of the optical spectra. J. H. thanks George Younes for useful discussions on the nature of the source.

B. O. is supported by the McWilliams Postdoctoral Fellowship at Carnegie Mellon University. J. H. acknowledges support from NASA under award number 80GSFC21M0002. P. B. is supported by a grant (no. 2020747) from the United States-Israel Binational Science Foundation (BSF), Jerusalem, Israel, by a grant (no. 1649/23) from the Israel Science Foundation and by a grant (no. 80NSSC 24K0770) from the NASA astrophysics theory program. M.N. is a Fonds de Recherche du Quebec—Nature et Technologies (FRQNT) postdoctoral fellow. S. S. is partially supported by LBNL Subcontract 7707915. G. B. acknowledges funding from the European Union's Horizon 2020 program under the AHEAD2020 project (grant agreement no. 871158). Research at Perimeter Institute is supported in part by the Government of Canada through the Department of Innovation, Science and Economic Development and by the Province of Ontario through the Ministry of Colleges and Universities.

The National Radio Astronomy Observatory is a facility of the National Science Foundation operated under cooperative agreement by Associated Universities, Inc. Based on observations obtained at the international Gemini Observatory, a program of NSF's OIR Lab, which is managed by the Association of Universities for Research in Astronomy (AURA) under a cooperative agreement with the National Science Foundation on behalf of the Gemini Observatory partnership: the National Science Foundation (United States), National Research Council (Canada), Agencia Nacional de Investigación y Desarrollo (Chile), Ministerio de Ciencia, Tecnologìa e Innovación (Argentina), Ministério da Ciência, Tecnologia, Inovações e Comunicações (Brazil), and Korea Astronomy and Space Science Institute (Republic of Korea). This work is based on observations obtained with the Southern African Large Telescope.

This research has made use of the NuSTAR Data Analysis Software (NuSTARDAS) jointly developed by the ASI Space Science Data Center (SSDC, Italy) and the California Institute of Technology (Caltech, USA). This work made use of data supplied by the UK Swift Science Data Centre at the University

of Leicester. This research has made use of the XRT Data Analysis Software (XRTDAS) developed under the responsibility of the ASI Science Data Center (ASDC), Italy. This research has made use of data and/or software provided by the High Energy Astrophysics Science Archive Research Center (HEASARC), which is a service of the Astrophysics Science Division at NASA/GSFC. Some of the data presented herein were obtained at the W. M. Keck Observatory, which is operated as a scientific partnership among the California Institute of Technology, the University of California and the National Aeronautics and Space Administration.

The Observatory was made possible by the generous financial support of the W. M. Keck Foundation. The authors wish to recognize and acknowledge the very significant cultural role and reverence that the summit of Maunakea has always had within the indigenous Hawaiian community. The Australia Telescope Compact Array is part of the Australia Telescope National Facility, which is funded by the Australian Government for operation as a National Facility managed by CSIRO. We acknowledge the Gomeroi people as the Traditional Owners of the Observatory site.

Facilities: NuSTAR, NICER, Swift, Gemini, Keck, DECam, VLA, ATCA

Software: `HEASoft`, `XRTDAS`, `NuSTARDAS`, `NICERDAS`, `XSPEC` (K. A. Arnaud 1996), `Dragons` (K. Labrie et al. 2019, 2023), `SFFT` (L. Hu et al. 2022), `IRAF` (D. Tody 1986), `CASA` (J. P. McMullin et al. 2007), `MIRIAD` (R. J. Sault et al. 1995), `pysynphot` (STScI Development Team 2013), `Astropy` (Astropy Collaboration et al. 2018).

Appendix A
Log of Observations

Here, we present the log of X-ray, ultraviolet, optical, infrared, and radio observations analyzed in this work (see Tables A1, A2, and A3).

Table A1
Log of X-Ray Observations Used in This Work

Start Time (UT)	δ (d)	Telescope	Instrument	Exposure (s)	ObsID
2024-04-10 13:33:08.00	1.82	NICER	XTI	2216	7204340101
2024-04-11 00:23:30.00	2.27	NICER	XTI	6064	7204340102
2024-04-12 01:10:19.00	3.30	NICER	XTI	8807	7204340103
2024-04-13 00:25:23.00	4.27	NICER	XTI	5277	7204340104
2024-04-14 01:10:54.00	5.30	NICER	XTI	4856	7204340105
2024-04-15 00:24:35.00	6.30	NICER	XTI	3488	7204340106
2024-04-16 16:40:37.00	7.94	NICER	XTI	331	7204340107
2024-04-17 01:57:57.00	8.33	NICER	XTI	831	7204340108
2024-04-18 01:11:16.00	9.30	NICER	XTI	2455	7204340109
2024-04-19 01:57:39.00	10.33	NICER	XTI	1560	7204340110
2024-04-20 01:08:00.00	11.30	NICER	XTI	4405	7204340111
2024-04-21 00:22:56.00	12.27	NICER	XTI	4398	7204340112
2024-04-22 01:10:20.00	13.30	NICER	XTI	4171	7204340113
2024-04-23 00:23:00.00	14.27	NICER	XTI	2700	7204340114
2024-04-24 01:08:00.00	15.30	NICER	XTI	2334	7204340115
2024-04-25 00:21:39.00	16.27	NICER	XTI	3136	7204340116
2024-04-26 04:12:59.00	17.43	NICER	XTI	6647	7204340117
2024-04-27 00:20:01.00	18.27	NICER	XTI	8229	7204340118
2024-04-28 01:04:49.00	19.29	NICER	XTI	5443	7204340119
2024-04-29 00:17:30.00	20.27	NICER	XTI	6846	7204340120
2024-04-30 01:00:00.00	21.29	NICER	XTI	4611	7204340121
2024-05-01 00:12:40.00	22.26	NICER	XTI	6797	7204340122
2024-05-02 01:02:00.00	23.30	NICER	XTI	4070	7204340123
2024-05-03 00:15:40.00	24.26	NICER	XTI	2939	7204340124
2024-05-09 03:38:01.00	30.40	NICER	XTI	251	7204340125
2024-05-10 22:32:07.00	32.19	NICER	XTI	468	7204340126
2024-05-11 00:05:07.00	32.26	NICER	XTI	1378	7204340127
2024-05-12 00:50:29.00	33.29	NICER	XTI	1312	7204340128
2024-05-14 11:39:20.00	35.74	NICER	XTI	1151	7204340129
2024-05-15 09:19:19.00	36.64	NICER	XTI	948	7204340130
2024-05-16 10:05:40.00	37.67	NICER	XTI	883	7204340131
2024-04-10 02:54:18	1.40	Swift	XRT	1825	16599001
2024-04-19 03:38:43	10.40	Swift	XRT	1015	16599003
2024-04-21 03:00:57	12.38	Swift	XRT	2648	16599004
2024-04-24 03:50:57	15.41	Swift	XRT	965	16599005
2024-04-26 04:37:57	17.45	Swift	XRT	2451	16599006
2024-04-22 00:36:09	13.28	NuSTAR	FPMA/B	42553	91001622002

Table A2
Log of Optical and Near-infrared Observations Used in This Work

Start Time (UT)	δT (d)	Telescope	Instrument	Exposure (s)	Filter	Transient (mag)	Candidate Host (mag)	A_λ (mag)
Gemini								
2024-04-25 03:34:24	16.40	Gemini	GMOS-S	720	*r*	>25.1[a]	⋯	0.21
2024-04-25 03:57:56	16.42	Gemini	GMOS-S	720	*i*	>25.0[a]	⋯	0.16
2024-04-25 04:31:40	16.44	Gemini	F2	900	*J*	>23.1[a]	⋯	0.07
2024-05-02 23:05:38	24.21	Gemini	GMOS-S	720	*r*	>25.5[a]	⋯	0.21
2024-05-02 23:25:34	24.23	Gemini	GMOS-S	720	*i*	>25.6[a]	⋯	0.16
2024-05-03 23:02:58	25.21	Gemini	F2	900	*J*	>23.2	>23.2	0.07
2024-06-30 00:29:04	82.27	Gemini	GMOS-S	960	*r*	>26.0[b]	24.2 ± 0.1	0.21
2024-06-30 00:59:36	82.29	Gemini	GMOS-S	1000	*i*	>26.1[b]	23.9 ± 0.1	0.16
UVOT								
2024-04-10 03:08:42	1.38	Swift	UVOT	157	*v*	>19.23	>19.23	0.25
2024-04-10 03:01:52	1.38	Swift	UVOT	157	*b*	>20.16	>20.16	0.32
2024-04-10 03:00:28	1.38	Swift	UVOT	157	*u*	>20.96	>20.96	0.40
2024-04-10 02:57:44	1.38	Swift	UVOT	314	*uvw1*	>20.99	>20.99	0.56
2024-04-10 03:10:07	1.38	Swift	UVOT	331	*uvm2*	>21.54	>21.54	0.71
2024-04-10 03:03:18	1.38	Swift	UVOT	629	*uvw2*	>22.18	>22.18	0.64
2024-04-20 03:26:05	11.4	Swift	UVOT	108	*u*	>20.73	>20.73	0.40
2024-04-19 03:41:31	10.41	Swift	UVOT	884	*uvw1*	>20.02	>20.02	0.56
2024-04-21 03:00:57	12.38	Swift	UVOT	2598	*uvw2*	>22.94	>22.94	0.64
2024-04-24 03:50:57	15.41	Swift	UVOT	994	*u*	>22.11	>22.11	0.40
2024-04-26 04:37:57	18.42	Swift	UVOT	2181	*uvw1*	>22.42	>22.42	0.56
2024-04-27 04:08:18	18.42	Swift	UVOT	228	*uvm2*	>21.23	>21.23	0.71
Stacked UVOT								
2024-04-10 02:54:18	1.4-12.4	Swift	UVOT	3227	*uvw2*	>23.1	>23.1	0.64
2024-04-10 02:54:18	1.4-18.4	Swift	UVOT	559	*uvm2*	>21.9	>21.9	0.71
2024-04-10 02:54:18	1.4-18.4	Swift	UVOT	3379	*uvw1*	>22.7	>22.7	0.56
2024-04-10 02:54:18	1.4-15.4	Swift	UVOT	1259	*u*	>22.2	>22.2	0.40

Notes. Photometry is reported in the AB magnitude system and is not corrected for Galactic extinction, which is tabulated for each filter in the A_λ column corresponding to the line-of-sight Galactic extinction of $E(B-V) = 0.076$ mag (E. F. Schlafly & D. P. Finkbeiner 2011). Upper limits are reported at 3σ.
[a] Upper limits from `SFFT` image subtraction.
[b] Upper limits from a source-free region within the XRT localization.

Table A3
Log of Radio Observations Used in This Work

Start Date (UT)	δT (d)	Telescope	Configuration	Band	Exposure (s)	Flux Density (μJy)
2024-04-19 02:08:22	10.34	VLA	C	X (10 GHz)	1410	< 17
2024-05-01 04:51:05	22.45	ATCA	⋯	C (5.5 GHz)	5760	< 60
2024-05-01 04:51:05	22.45	ATCA	⋯	X (9 GHz)	5760	< 60
2024-05-10 06:39:45	31.53	ATCA	⋯	K (18 GHz)	5400	< 180[a]
2024-09-13 17:40:28	158.0	VLA	B	X (10 GHz)	1410	< 21
2024-12-12 10:29:00	247.7	VLA	A	X (10 GHz)	1410	< 20

Note. Upper limits are reported at the 3σ level.
[a] This is a rough estimate of the upper limit at this epoch in a merged observation; see Section 2.11 for caveats.

Appendix B
Timing Analysis/Pulsations Search on NICER Data

We conducted an X-ray pulsation search in the event that a neutron star is responsible for the transient event, such as an MSP or a magnetar. In particular, we utilized the acceleration search, a Fourier domain technique that accounts for the "smearing" of a potential coherent signal due to the orbital Doppler modulation (S. M. Ransom et al. 2002). In Fourier space, the signal would be smeared across $z = \alpha h f T^2/c$ Fourier bins, where α is the pulsar acceleration, h is the harmonic number ($h = 1$ is the fundamental), f is the potential pulse frequency, T is the length of the time segment being searched over, and c is the speed of light (S. M. Ransom et al. 2002). Acceleration searches are optimal when the pulsar acceleration is roughly constant within time segments such that $T \leqslant P_{\rm orb}/10$, where $P_{\rm orb}/10$ is the orbital period of the binary system. We note that for isolated pulsars (e.g., a magnetar), $z = 0$. We employed the `accelsearch` routine as implemented within version 4.0 of `PRESTO`[51] for the acceleration search (S. M. Ransom et al. 2002; S. Ransom

[51] https://github.com/scottransom/presto

2011), searching over 0.5–1000 Hz and between 0.5–2.0 keV and 2.0–10.0 keV. We also searched up to a maximum of 100 bins in Fourier frequency space that the Doppler-modulated signal would drift across. We did not find any significant periodicity candidates from the acceleration search.

We also constructed an averaged power spectrum using the `AveragedPowerspectrum` class in `Stingray` (D. Huppenkothen et al. 2019a, 2019b), where we used 256 s bins and a bin size of $\Delta t = 2^{-12}$ s. We did not find any significant coherent periodicity in the averaged spectrum, and we determined a 3σ upper limit on the sinusoidal pulsation amplitude of 24.5–27.0% over 1–1000 Hz (B. A. Vaughan et al. 1994).

Appendix C
Notes on Candidate Optical Counterparts

The bright source reported by A. Rau (2024) appears point-like in our images (Figure 1), indistinguishable from the numerous field stars in our deep Gemini images. While this source lies in the initial XRT position, it is no longer consistent with the updated enhanced position (Figure 1). In any case, the broad absorption features observed in our Gemini spectrum (Figure A1, left panel) between 6000 and 7000 Å are indicative of a stellar spectrum. N. Rea et al. (2024a) carried out follow-up spectroscopy with SALT and reported a potential emission line from this source. However, a reanalysis of the spectrum shows that this is unrelated to this source.

We compared the ultraviolet, optical, and near-infrared spectral energy distribution (SED) to stellar models (R. L. Kurucz 1993) using `pysynphot` (STScI Development Team 2013). We find an appropriate match to the SED for a late spectral type dwarf of type between M2V and M4V located at a distance of $\sim$2 kpc. We consider an M dwarf with temperature 3500 K and metallicity $\log(Z/Z_\odot) = -2$ (solid line), with temperature 3600 K with $\log(Z/Z_\odot) = -0.5$ (dashed line), and with temperature 3800 K with $\log(Z/Z_\odot) = 0.5$ (dotted line). This SED comparison is shown in Figure A1 (right panel). This conclusively confirms the source is unrelated to EP240408a.

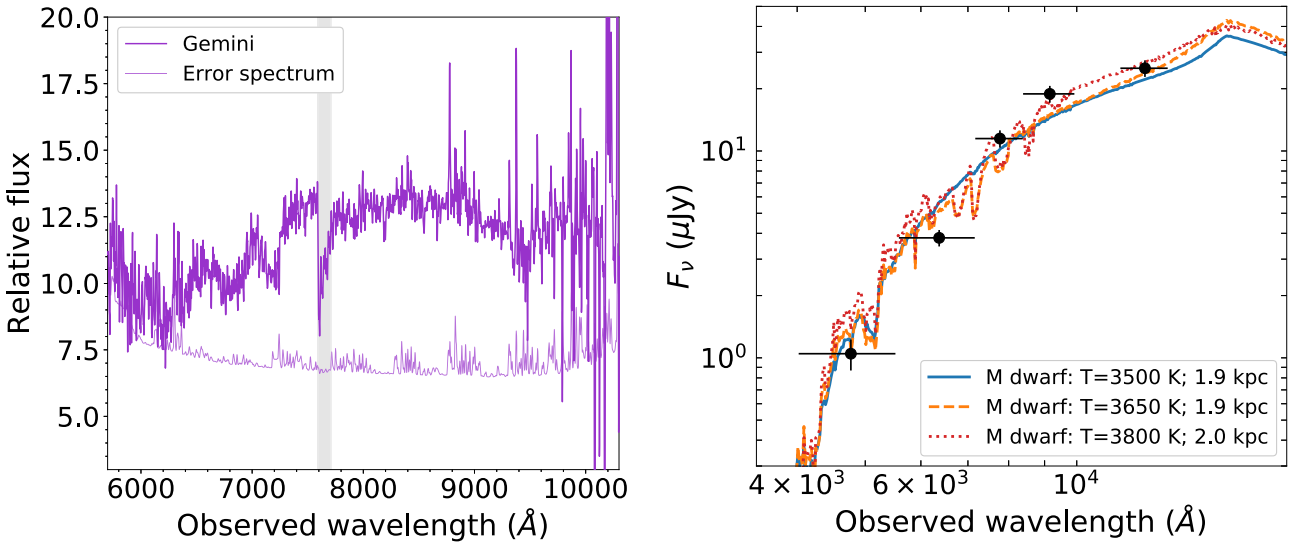

Figure A1. Left: Gemini GMOS-S optical spectrum of the bright source (A. Rau 2024) lying within the initial (standard) XRT localization. The error spectrum is also shown. The spectrum is smoothed with a Savitzky–Golay filter of 3 pixels for display purposes. Vertical gray shaded regions mark atmospheric telluric absorption regions. The sharp peaks in the observed spectrum above 8, 600 Å are due to sky emission lines and are not real features. Right: SED of this source (A. Rau 2024) compared to Kurucz stellar models (R. L. Kurucz 1993). We find adequate matches to the observed photometry corresponding to late spectral type M dwarfs at $\sim$ 2 kpc. The models are extincted by $E(B-V) = 0.076$ mag (E. F. Schlafly & D. P. Finkbeiner 2011).

ORCID iDs

Brendan O'Connor https://orcid.org/0000-0002-9700-0036
Dheeraj Pasham https://orcid.org/0000-0003-1386-7861
Igor Andreoni https://orcid.org/0000-0002-8977-1498
Jeremy Hare https://orcid.org/0000-0002-8548-482X
Paz Beniamini https://orcid.org/0000-0001-7833-1043
Eleonora Troja https://orcid.org/0000-0002-1869-7817
Roberto Ricci https://orcid.org/0000-0003-4631-1528
Dougal Dobie https://orcid.org/0000-0003-0699-7019
Joheen Chakraborty https://orcid.org/0000-0002-0568-6000
Mason Ng https://orcid.org/0000-0002-0940-6563
Noel Klingler https://orcid.org/0000-0002-0786-7307
Viraj Karambelkar https://orcid.org/0000-0003-2758-159X
Sam Rose https://orcid.org/0000-0003-4725-4481
Steve Schulze https://orcid.org/0000-0001-6797-1889
Geoffrey Ryan https://orcid.org/0000-0001-9068-7157
Simone Dichiara https://orcid.org/0000-0001-6849-1270
Itumeleng Monageng https://orcid.org/0000-0002-4754-3526
David Buckley https://orcid.org/0000-0002-7004-9956
Lei Hu https://orcid.org/0000-0001-7201-1938
Gokul P. Srinivasaragavan https://orcid.org/0000-0002-6428-2700
Gabriele Bruni https://orcid.org/0000-0002-5182-6289
Tomás Cabrera https://orcid.org/0000-0002-1270-7666
S. Bradley Cenko https://orcid.org/0000-0003-1673-970X
Hendrik van Eerten https://orcid.org/0000-0002-8680-8718
James Freeburn https://orcid.org/0009-0006-7990-0547
Erica Hammerstein https://orcid.org/0000-0002-5698-8703
Mansi Kasliwal https://orcid.org/0000-0002-5619-4938
Chryssa Kouveliotou https://orcid.org/0000-0003-1443-593X
Keerthi Kunnumkai https://orcid.org/0009-0000-4830-1484
James K. Leung https://orcid.org/0000-0002-9415-3766
Amy Lien https://orcid.org/0000-0002-7851-9756
Antonella Palmese https://orcid.org/0000-0002-6011-0530
Takanori Sakamoto https://orcid.org/0000-0001-6276-6616

References

Abbott, B. P., Abbott, R., Abbott, T. D., et al. 2017, ApJL, 848, L12
Ai, S., & Zhang, B. 2021, ApJL, 915, L11
Alp, D., & Larsson, J. 2020, ApJ, 896, 39
Andreoni, I., Coughlin, M. W., Perley, D. A., et al. 2022, Natur, 612, 430
Aptekar, R. L., Frederiks, D. D., Golenetskii, S. V., et al. 1995, SSRv, 71, 265
Arnaud, K. A. 1996, in ASP Conf. Ser. 101, Astronomical Data Analysis Software and Systems V, ed. G. H. Jacoby & J. Barnes (San Francisco, CA: ASP), 17
Astropy Collaboration, Price-Whelan, A. M., Sipőcz, B. M., et al. 2018, AJ, 156, 123
Atteia, J. L., Heussaff, V., Dezalay, J. P., et al. 2017, ApJ, 837, 119
Band, D., Matteson, J., Ford, L., et al. 1993, ApJ, 413, 281
Barniol Duran, R. 2014, MNRAS, 442, 3147
Barniol Duran, R., Nakar, E., & Piran, T. 2013, ApJ, 772, 78
Barniol Duran, R., & Piran, T. 2013, ApJ, 770, 146
Barthelmy, S. D., Barbier, L. M., Cummings, J. R., et al. 2005, SSRv, 120, 143
Bauer, F. E., Treister, E., Schawinski, K., et al. 2017, MNRAS, 467, 4841
Beniamini, P., Duque, R., Daigne, F., & Mochkovitch, R. 2020a, MNRAS, 492, 2847
Beniamini, P., Duran, R. B., Petropoulou, M., & Giannios, D. 2020b, ApJL, 895, L33
Beniamini, P., Giannios, D., & Metzger, B. D. 2017, MNRAS, 472, 3058
Beniamini, P., & Kumar, P. 2016, MNRAS, 457, L108
Beniamini, P., & Mochkovitch, R. 2017, A&A, 605, A60
Beniamini, P., & Nakar, E. 2019, MNRAS, 482, 5430
Beniamini, P., Nava, L., Duran, R. B., & Piran, T. 2015, MNRAS, 454, 1073
Beniamini, P., Piran, T., & Matsumoto, T. 2023, MNRAS, 524, 1386
Beniamini, P., & van der Horst, A. J. 2017, MNRAS, 472, 3161
Berger, E. 2010a, ApJ, 722, 1946
Berger, E. 2014, ARA&A, 52, 43
Bertin, E., & Arnouts, S. 1996, A&AS, 117, 393
Bhalerao, V., Bhattacharya, D., Vibhute, A., et al. 2017, JApA, 38, 31
Bloom, J. S., Kulkarni, S. R., & Djorgovski, S. G. 2002, AJ, 123, 1111
Bloom, J. S., Giannios, D., Metzger, B. D., et al. 2011, Sci, 333, 203
Bright, J. S., Carotenuto, F., Fender, R., et al. 2024, arXiv:2409.19055
Brown, G. C., Levan, A. J., Stanway, E. R., et al. 2015, MNRAS, 452, 4297
Burrows, D. N., Hill, J. E., Nousek, J. A., et al. 2005, SSRv, 120, 165
Burrows, D. N., Kennea, J. A., Ghisellini, G., et al. 2011, Natur, 476, 421
Cano, Z., Wang, S.-Q., Dai, Z.-G., & Wu, X.-F. 2017, AdAst, 2017, 8929054
Cash, W. 1979, ApJ, 228, 939
Cendes, Y., Berger, E., Alexander, K. D., et al. 2022, ApJ, 938, 28
Cendes, Y., Berger, E., Alexander, K. D., et al. 2024, ApJ, 971, 185
Cenko, S. B., Krimm, H. A., Horesh, A., et al. 2012, ApJ, 753, 77
Chabrier, G. 2003, PASP, 115, 763
Chandra, A. D. 2024, ATel, 16585
Chandra, P., & Frail, D. A. 2012, ApJ, 746, 156
Chen, W., Xie, W., Lei, W.-H., et al. 2017, ApJ, 849, 119
Chevalier, R. A., & Li, Z.-Y. 2000, ApJ, 536, 195
Coppejans, D. L., Margutti, R., Terreran, G., et al. 2020, ApJL, 895, L23
Coti Zelati, F., Rea, N., Turolla, R., et al. 2017, MNRAS, 471, 1819
Cucchiara, A., Veres, P., Corsi, A., et al. 2015, ApJ, 812, 122
Cummings, J. R., Barthelmy, S. D., Beardmore, A. P., et al. 2011, GCN, 11823, 1
Dainotti, M. G., De Simone, B., Malik, R. F. M., et al. 2024, MNRAS, 533, 4023
Dalal, N., Griest, K., & Pruet, J. 2002, ApJ, 564, 209
DeLaunay, J., & Tohuvavohu, A. 2022, ApJ, 941, 169
Della Valle, M., Chincarini, G., Panagia, N., et al. 2006, Natur, 444, 1050
Dereli-Bégué, H., Pe'er, A., Ryde, F., et al. 2022, NatCo, 13, 5611
Dichiara, S., Tsang, D., Troja, E., et al. 2023, ApJL, 954, L29
Donnarumma, I., Vittorini, V., Vercellone, S., et al. 2009, ApJL, 691, L13
Drout, M. R., Chornock, R., Soderberg, A. M., et al. 2014, ApJ, 794, 23
Duffell, P. C., & MacFadyen, A. I. 2015, ApJ, 806, 205
Duncan, R. A., van der Horst, A. J., & Beniamini, P. 2023, MNRAS, 518, 1522
Duncan, R. C., & Thompson, C. 1992, ApJL, 392, L9
Eappachen, D., Jonker, P. G., Levan, A. J., et al. 2023, ApJ, 948, 91
Eftekhari, T., Berger, E., Zauderer, B. A., Margutti, R., & Alexander, K. D. 2018, ApJ, 854, 86
Eftekhari, T., Tchekhovskoy, A., Alexander, K. D., et al. 2024, ApJ, 974, 149
Evans, P. A., Page, K. L., Bearmore, A. P., et al. 2023, MNRAS, 518, 174
Evans, P. A., Beardmore, A. P., Page, K. L., et al. 2009, MNRAS, 397, 1177
Falanga, M., Kuiper, L., Poutanen, J., et al. 2005, A&A, 444, 15
Fong, W., Berger, E., Chornock, R., et al. 2013, ApJ, 769, 56
Fong, W.-f., Nugent, A. E., Dong, Y., et al. 2022, ApJ, 940, 56
Frail, D. A., Kulkarni, S. R., Sari, R., et al. 2001, ApJL, 562, L55
Gal-Yam, A., Fox, D. B., Price, P. A., et al. 2006, Natur, 444, 1053
Galama, T. J., Vreeswijk, P. M., van Paradijs, J., et al. 1998, Natur, 395, 670
Gao, H.-X., Geng, J.-J., Wu, X.-F., et al. 2024, arXiv:2410.21687
Gaudin, T. M., Coe, M. J., Kennea, J. A., et al. 2024, MNRAS, 534, 1937
Gehrels, N., Chincarini, G., Giommi, P., et al. 2004, ApJ, 611, 1005
Gendreau, K. C., Arzoumanian, Z., Adkins, P. W., et al. 2016, Proc. SPIE, 9905, 99051H
Ghirlanda, G., & Salvaterra, R. 2022, ApJ, 932, 10
Ghirlanda, G., Ghisellini, G., Nava, L., et al. 2012, MNRAS, 422, 2553
Ghirlanda, G., Nappo, F., Ghisellini, G., et al. 2018, A&A, 609, A112
Ghisellini, G., Ghirlanda, G., Nava, L., & Celotti, A. 2010, MNRAS, 403, 926
Giacomazzo, B., & Perna, R. 2013, ApJL, 771, L26
Gilfanov, M., Revnivtsev, M., Sunyaev, R., & Churazov, E. 1998, A&A, 338, L83
Gill, R., Granot, J., & Kumar, P. 2020, MNRAS, 491, 3343
Gillanders, J. H., Troja, E., Fryer, C. L., et al. 2023, arXiv:2308.00633
Gillanders, J. H., Rhodes, L., Srivastav, S., et al. 2024, ApJL, 969, L14
Glennie, A., Jonker, P. G., Fender, R. P., Nagayama, T., & Pretorius, M. L. 2015, MNRAS, 450, 3765
Goad, M. R., Tyler, L. G., Beardmore, A. P., et al. 2007, A&A, 476, 1401
Goldstein, A., Veres, P., Burns, E., et al. 2017, ApJL, 848, L14
Gompertz, B. P., O'Brien, P. T., & Wynn, G. A. 2014, MNRAS, 438, 240
Gompertz, B. P., Ravasio, M. E., Nicholl, M., et al. 2023, NatAs, 7, 67
Granot, J., Piran, T., Bromberg, O., Racusin, J. L., & Daigne, F. 2015, SSRv, 191, 471
Granot, J., & Sari, R. 2002, ApJ, 568, 820
Guillochon, J., & Ramirez-Ruiz, E. 2013, ApJ, 767, 25
Güver, T., & Özel, F. 2009, MNRAS, 400, 2050
Hamil, O., Stone, J. R., Urbanec, M., & Urbancová, G. 2015, PhRvD, 91, 063007
Hammerstein, E., Gezari, S., van Velzen, S., et al. 2021, ApJL, 908, L20

Hjorth, J., & Bloom, J. S. 2012, in Chapter 9 in "Gamma-Ray Bursts, ed. C. Kouveliotou, R. A. M. J. Wijers, & S. Woosley (Cambridge: Cambridge Univ. Press), 169
Ho, A. Y. Q., Phinney, E. S., Ravi, V., et al. 2019, ApJ, 871, 73
Ho, A. Y. Q., Perley, D. A., Kulkarni, S. R., et al. 2020a, ApJ, 895, 49
Ho, A. Y. Q., Perley, D. A., Beniamini, P., et al. 2020b, ApJ, 905, 98
Ho, A. Y. Q., Perley, D. A., Chen, P., et al. 2023, Natur, 623, 927
Horesh, A., Cenko, S. B., & Arcavi, I. 2021a, NatAs, 5, 491
Horesh, A., Sfaradi, I., Fender, R., et al. 2021b, ApJL, 920, L5
Hu, J. W., Zhao, D. H., Liu, Y., et al. 2024a, GCN, 36053, 1
Hu, J. W., Zhao, D. H., Liu, Y., et al. 2024b, GCN, 36057, 1
Hu, L., Wang, L., Chen, X., & Yang, J. 2022, ApJ, 936, 157
Huang, Y. F., Dai, Z. G., & Lu, T. 2002, MNRAS, 332, 735
Huppenkothen, D., Bachetti, M., Stevens, A. L., et al. 2019a, ApJ, 881, 39
Huppenkothen, D., Bachetti, M., Stevens, A., et al. 2019b, JOSS, 4, 1393
Jonker, P. G., Miller-Jones, J., Homan, J., et al. 2010, MNRAS, 401, 1255
Jonker, P. G., Glennie, A., Heida, M., et al. 2013, ApJ, 779, 14
Keller, S. C., Schmidt, B. P., Bessell, M. S., et al. 2007, PASA, 24, 1
Kochanek, C. S. 2016, MNRAS, 461, 371
König, O., Saxton, R. D., Kretschmar, P., et al. 2022, A&C, 38, 100529
Kouveliotou, C., Meegan, C. A., Fishman, G. J., et al. 1993, ApJL, 413, L101
Kraft, R. P., Burrows, D. N., & Nousek, J. A. 1991, ApJ, 374, 344
Krimm, H. A., Holland, S. T., Corbet, R. H. D., et al. 2013, ApJS, 209, 14
Kumar, P., & Panaitescu, A. 2000, ApJL, 541, L51
Kurucz, R. L. 1993, yCat, VI/39,
Labrie, K., Anderson, K., Cárdenes, R., Simpson, C., & Turner, J. E. H. 2019, in ASP Conf. Ser. 523, Astronomical Data Analysis Software and Systems XXVII, ed. P. J. Teuben, M. W. Pound, B. A. Thomas, & E. M. Warner (San Francisco, CA: ASP), 321
Labrie, K., Simpson, C., Cardenes, R., et al. 2023, RNAAS, 7, 214
Laskar, T., Escorial, A. R., Schroeder, G., et al. 2022, ApJL, 935, L11
Lattimer, J. M., & Prakash, M. 2004, Sci, 304, 536
Levan, A., Gompertz, B. P., Salafia, O. S., et al. 2024, Natur, 626, 737
Levan, A. J., Tanvir, N. R., Cenko, S. B., et al. 2011, Sci, 333, 199
Levan, A. J., Tanvir, N. R., Starling, R. L. C., et al. 2014, ApJ, 781, 13
Levan, A. J., Tanvir, N. R., Brown, G. C., et al. 2016, ApJ, 819, 51
Levan, A. J., Jonker, P. G., Saccardi, A., et al. 2024, arXiv:2404.16350
Li, C., Peng, W., Liu, Y., et al. 2023, ExA, 56, 49
Liang, E. W., Zhang, B., O'Brien, P. T., et al. 2006, ApJ, 646, 351
Lien, A., Sakamoto, T., Barthelmy, S. D., et al. 2016, ApJ, 829, 7
Liu, Y., Sun, H., Xu, D., et al. 2024, arXiv:2404.16425
Lü, H.-J., Zhang, B., Lei, W.-H., Li, Y., & Lasky, P. D. 2015, ApJ, 805, 89
Lyons, N., O'Brien, P. T., Zhang, B., et al. 2010, MNRAS, 402, 705
MacFadyen, A. I., & Woosley, S. E. 1999, ApJ, 524, 262
Mangano, V., Burrows, D. N., Sbarufatti, B., & Cannizzo, J. K. 2016, ApJ, 817, 103
Margutti, R., Metzger, B. D., Chornock, R., et al. 2019, ApJ, 872, 18
Margutti, R., J, N. A., Chornock, R., et al. 2024, TNSAN, 214, 1
Markwardt, C. B., Swank, J. H., Strohmayer, T. E., in 't Zand, J. J. M., & Marshall, F. E. 2002, ApJL, 575, L21
Matsumoto, T., Nakar, E., & Piran, T. 2019, MNRAS, 483, 1247
Matsumoto, T., & Piran, T. 2023, MNRAS, 522, 4565
McManus, S., & Olsen, K. 2021, Mirro, 2, 33
McMullin, J. P., Waters, B., Schiebel, D., Young, W., & Golap, K. 2007, in ASP Conf. Ser. 376, Astronomical Data Analysis Software and Systems XVI, ed. R. A. Shaw, F. Hill, & D. J. Bell (San Francisco, CA: ASP), 127
Meegan, C., Lichti, G., Bhat, P. N., et al. 2009, ApJ, 702, 791
Mészáros, P., & Rees, M. J. 1997, ApJ, 476, 232
Metzger, B. D., Giannios, D., Thompson, T. A., Bucciantini, N., & Quataert, E. 2011, MNRAS, 413, 2031
Molinari, E., Vergani, S. D., Malesani, D., et al. 2007, A&A, 469, L13
Nakar, E., & Piran, T. 2011, Natur, 478, 82
Nakar, E., Piran, T., & Granot, J. 2002, ApJ, 579, 699
Nappo, F., Ghisellini, G., Ghirlanda, G., et al. 2014, MNRAS, 445, 1625
Nauenberg, M. 1972, ApJ, 175, 417
Nava, L., Sironi, L., Ghisellini, G., Celotti, A., & Ghirlanda, G. 2013, MNRAS, 433, 2107
Nicholl, M., Berger, E., Kasen, D., et al. 2017, ApJL, 848, L18
Nugent, A. E., Fong, W.-F., Dong, Y., et al. 2022, ApJ, 940, 57
Nysewander, M., Fruchter, A. S., & Pe'er, A. 2009, ApJ, 701, 824
O'Connor, B., Beniamini, P., & Gill, R. 2024, MNRAS, 553, 1629
O'Connor, B., Beniamini, P., & Kouveliotou, C. 2020, MNRAS, 495, 4782
O'Connor, B., Troja, E., Dichiara, S., et al. 2022, MNRAS, 515, 4890
O'Connor, B., Troja, E., Ryan, G., et al. 2023, SciA, 9, eadi1405
Oganesyan, G., Ascenzi, S., Branchesi, M., et al. 2020, ApJ, 893, 88
Palmerio, J. T., Vergani, S. D., Salvaterra, R., et al. 2019, A&A, 623, A26
Panaitescu, A., & Kumar, P. 2003, ApJ, 592, 390
Parsotan, T., & Lazzati, D. 2024, ApJ, 974, 158
Pasham, D. R., Cenko, S. B., Levan, A. J., et al. 2015, ApJ, 805, 68
Pasham, D. R., Lucchini, M., Laskar, T., et al. 2023, NatAs, 7, 88
Perley, D. A., Metzger, B. D., Granot, J., et al. 2009, ApJ, 696, 1871
Perley, D. A., Mazzali, P. A., Yan, L., et al. 2019, MNRAS, 484, 1031
Perley, D. A., Ho, A. Y. Q., Yao, Y., et al. 2021, MNRAS, 508, 5138
Perley, D. A., Ho, A. Y. Q., Fausnaugh, M., et al. 2024, arXiv:2401.16470
Perlman, E. S., Meyer, E. T., Wang, Q. D., et al. 2022, ApJ, 925, 143
Pineau, F. X., Motch, C., Carrera, F., et al. 2011, A&A, 527, A126
Piran, T., & Beniamini, P. 2023, JCAP, 2023, 049
Planck Collaboration, Aghanim, N., Akrami, Y., et al. 2020, A&A, 641, A6
Potter, S. B., Buckley, D. A. H., Scaringi, S., et al. 2024, MNRAS, 532, L21
Prentice, S. J., Maguire, K., Smartt, S. J., et al. 2018, ApJL, 865, L3
Prochaska, J., Hennawi, J., Westfall, K., et al. 2020, JOSS, 5, 2308
Pursiainen, M., Childress, M., Smith, M., et al. 2018, MNRAS, 481, 894
Quirola-Vásquez, J., Bauer, F. E., Jonker, P. G., et al. 2022, A&A, 663, A168
Quirola-Vásquez, J., Bauer, F. E., Jonker, P. G., et al. 2023, A&A, 675, A44
Quirola-Vásquez, J., Bauer, F. E., Jonker, P. G., et al. 2024a, A&A, 683, A243
Quirola-Vásquez, J., Bauer, F. E., Jonker, P. G., et al. 2024b, arXiv:2410.10015
Ransom, S., 2011 PRESTO: PulsaR Exploration and Search TOolkit, Astrophysics Source Code Library, ascl:1107.017
Ransom, S. M., Eikenberry, S. S., & Middleditch, J. 2002, AJ, 124, 1788
Rastinejad, J. C., Gompertz, B. P., Levan, A. J., et al. 2022, Natur, 612, 223
Rau, A. 2024, GCN, 36059, 1
Rea, N., Galbany, L., Coti Zelati, F., et al. 2024a, ATel, 16589, 1
Rea, N., Coti Zelati, F., Marino, A., et al. 2024b, ATel, 16584, 1
Rhoads, J. E. 1999, ApJ, 525, 737
Rhodes, L., Bright, J. S., Fender, R., et al. 2023, MNRAS, 521, 389
Ricci, R., Troja, E., Yang, Y., et al. 2024, arXiv:2407.18311
Ridnaia, A., Svinkin, D., & Frederiks, D. 2020, JPhCS, 1697, 012030
Roming, P. W. A., Kennedy, T. E., Mason, K. O., et al. 2005, SSRv, 120, 95
Rowlinson, A., O'Brien, P. T., Metzger, B. D., Tanvir, N. R., & Levan, A. J. 2013, MNRAS, 430, 1061
Rowlinson, A., O'Brien, P. T., Tanvir, N. R., et al. 2010, MNRAS, 409, 531
Ryan, G., van Eerten, H., MacFadyen, A., & Zhang, B.-B. 2015, ApJ, 799, 3
Sakamoto, T., Barthelmy, S. D., Baumgartner, W. H., et al. 2011a, ApJS, 195, 2
Sakamoto, T., Barthelmy, S. D., Baumgartner, W. H., et al. 2011b, GCN, 11842, 1
Sanna, A., Pintore, F., Riggio, A., et al. 2018, MNRAS, 481, 1658
Santana, R., Barniol Duran, R., & Kumar, P. 2014, ApJ, 785, 29
Sari, R., & Esin, A. A. 2001, ApJ, 548, 787
Sari, R., & Piran, T. 1999, ApJ, 520, 641
Sari, R., Piran, T., & Halpern, J. P. 1999, ApJL, 519, L17
Sari, R., Piran, T., & Narayan, R. 1998, ApJL, 497, L17
Sarin, N., Ashton, G., Lasky, P. D., et al. 2021, arXiv:2105.10108
Sault, R. J., Teuben, P. J., & Wright, M. C. H. 1995, in ASP Conf. Ser. 77, Astronomical Data Analysis Software and Systems IV, ed. R. A. Shaw, H. E. Payne, & J. J. E. Hayes (San Francisco, CA: ASP), 433
Savchenko, V., Ferrigno, C., Kuulkers, E., et al. 2017, ApJL, 848, L15
Saxton, R. D., Read, A. M., Esquej, P., et al. 2008, A&A, 480, 611
Saxton, R. D., König, O., Descalzo, M., et al. 2022, A&C, 38, 100531
Scargle, J. D., Norris, J. P., Jackson, B., & Chiang, J. 2013, ApJ, 764, 167
Schlafly, E. F., & Finkbeiner, D. P. 2011, ApJ, 737, 103
Schneider, B., Le Floc'h, E., Arabsalmani, M., Vergani, S. D., & Palmerio, J. T. 2022, A&A, 666, A14
Sfaradi, I., Horesh, A., Fender, R., et al. 2022, ApJ, 933, 176
Sfaradi, I., Beniamini, P., Horesh, A., et al. 2024, MNRAS, 527, 7672
Shen, R., & Matzner, C. D. 2012, ApJ, 744, 36
Skrutskie, M. F., Cutri, R. M., Stiening, R., et al. 2006, AJ, 131, 1163
Soderberg, A. M., Kulkarni, S. R., Nakar, E., et al. 2006, Natur, 442, 1014
Speagle, J. S. 2020, MNRAS, 493, 3132
Srinivasaragavan, G. P., O'Connor, B., Cenko, S. B., et al. 2023, ApJL, 949, L39
Srinivasaragavan, G. P., Swain, V., O'Connor, B., et al. 2024, ApJL, 960, L18
Srivastav, S., Chen, T. W., Gillanders, J. H., et al. 2024, arXiv:2409.19070
Stone, N., Sari, R., & Loeb, A. 2013, MNRAS, 435, 1809
Stone, N. C., & Metzger, B. D. 2016, MNRAS, 455, 859
STScIDevelopment Team, 2013 pysynphot: Synthetic photometry software package, Astrophysics Source Code Library, ascl:1303.023
Sun, H., Li, W. X., Liu, L. D., et al. 2024, arXiv:2410.02315
Tang, C.-H., Huang, Y.-F., Geng, J.-J., & Zhang, Z.-B. 2019, ApJS, 245, 1
Taylor, E. N., Cluver, M. E., Duffy, A., et al. 2020, MNRAS, 499, 2896
Teboul, O., & Metzger, B. D. 2023, ApJL, 957, L9

Tody, D. 1986, Proc. SPIE, 627, 733
Troja, E., Cusumano, G., O'Brien, P. T., et al. 2007, ApJ, 665, 599
Troja, E., Fryer, C. L., O'Connor, B., et al. 2022, Natur, 612, 228
Tubìn-Arenas, D., Krumpe, M., Lamer, G., et al. 2024, A&A, 682, A35
Ulmer, A. 1999, ApJ, 514, 180
Usov, V. V. 1992, Natur, 357, 472
Uttley, P., McHardy, I. M., Papadakis, I. E., Guainazzi, M., & Fruscione, A. 1999, MNRAS, 307, L6
Uttley, P., McHardy, I. M., & Vaughan, S. 2005, MNRAS, 359, 345
van Dalen, J. N. D., Levan, A. J., Jonker, P. G., et al. 2024, arXiv:2409.19056
van Eerten, H., Zhang, W., & MacFadyen, A. 2010, ApJ, 722, 235
van Velzen, S., Anderson, G. E., Stone, N. C., et al. 2016, Sci, 351, 62
Vaughan, B. A., van der Klis, M., Wood, K. S., et al. 1994, ApJ, 435, 362
Wang, C.-W., Xiong, S.-L., Liu, J.-C., et al. 2024, GCN, 36058, 1
Wichern, H. C. I., Ravasio, M. E., Jonker, P. G., et al. 2024, A&A, 690, A101
Wijers, R. A. M. J., & Galama, T. J. 1999, ApJ, 523, 177
Wijnands, R. 2004, in AIP Conf. Ser. 714, X-Ray Timing 2003: Rossi and Beyond, ed. P. Kaaret, F. K. Lamb, & J. H. Swank (Melville, NY: AIP), 209
Willingale, R., Starling, R. L. C., Beardmore, A. P., Tanvir, N. R., & O'Brien, P. T. 2013, MNRAS, 431, 394
Wilson, J. C., Henderson, C. P., Herter, T. L., et al. 2004, Proc. SPIE, 5492, 1295
Wolf, C., Onken, C. A., Luvaul, L. C., et al. 2018, PASA, 35, e010
Woosley, S. E. 1993, ApJ, 405, 273
Xu, F., Huang, Y.-F., Geng, J.-J., et al. 2023, A&A, 673, A20
Xu, F., Tang, C.-H., Geng, J.-J., et al. 2021, ApJ, 920, 135
Xue, Y. Q., Zheng, X. C., Li, Y., et al. 2019, Natur, 568, 198
Yang, B., Jin, Z.-P., Li, X., et al. 2015, NatCo, 6, 7323
Yang, J., Ai, S., Zhang, B.-B., et al. 2022, Natur, 612, 232
Yang, Y.-H., Troja, E., O'Connor, B., et al. 2024, Natur, 626, 742
Yao, Y., Lu, W., Harrison, F., et al. 2024, ApJ, 965, 39
Yao, Y., Ho, A. Y. Q., Medvedev, P., et al. 2022, ApJ, 934, 104
Ye, C. S., Fragione, G., & Perna, R. 2023, ApJ, 953, 141
Yi, S. X., Dai, Z. G., Wu, X. F., & Wang, F. Y. 2014, arXiv:1401.1601
Yin, Y.-H. I., Zhang, B.-B., Yang, J., et al. 2024, ApJL, 975, L27
Yuan, W., Zhang, C., Chen, Y., & Ling, Z. 2022, in Handbook of X-Ray and Gamma-Ray Astrophysics, ed. C. Bambi & A, Santangelo (Singapore: Springer), 86
Yuan, W., Zhang, C., Feng, H., et al. 2015, arXiv:1506.07735
Zauderer, B. A., Berger, E., Margutti, R., et al. 2013, ApJ, 767, 152
Zauderer, B. A., Berger, E., Soderberg, A. M., et al. 2011, Natur, 476, 425
Zhang, B., Fan, Y. Z., Dyks, J., et al. 2006, ApJ, 642, 354
Zhang, B., & Mészáros, P. 2001, ApJL, 552, L35
Zhang, B.-B., van Eerten, H., Burrows, D. N., et al. 2015, ApJ, 806, 15
Zhang, C., Ling, Z. X., Liu, Y., et al. 2024, ATel, 16463, 1
Zou, Y.-C., Fan, Y.-Z., & Piran, T. 2009, MNRAS, 396, 1163